Survey of the $(\alpha, {}^2\mathrm{He})$ reaction on fp-shell nuclei

U. Fister, R. Jahn, P. von Neumann-Cosel,* P. Schenk, T. K. Trelle, D. Wenzel, and U. Wienands†
Institut für Strahlen- und Kernphysik, Universität Bonn, D-5300 Bonn, Federal Republic of Germany
(Received 22 June 1990)

The $(\alpha, {}^2\mathrm{He})$ reaction has been investigated at bombarding energies around 56 MeV on targets of ^{40,42,44,48}Ca, ^{50,52,54}Cr, ^{54,56,58}Fe, ^{58,60,62,64}Ni, ^{64,66}Zn, and ^{70,72}Ge. The angular distributions of prominent two-neutron states were analyzed with the distorted-wave Born approximation. Preferential population of states with dominant $(f_{5/2},g_{9/2})_{7^-}$, $(g_{9/2})^2_{8^+}$, and $(g_{9/2},d_{5/2})_{6^+}$ configurations was observed for all nuclei with a closed $f_{7/2}$ neutron shell. The binding energies of the 7^-, 8^+, and 6^+ states are linearly dependent on the mass number and the isospin and well described by the weak-coupling model. The extracted parameters agree with the averaged values of a similar analysis for $f_{5/2}$, $g_{9/2}$, and $d_{5/2}$ single-particle states in the corresponding odd-even nuclei. The excitation energies of the high-spin states could be well reproduced by a simplified shell model where only pure configurations are considered and the residual interaction energy is neglected. The simple structure of the experimentally observed states is further tested by large-scale shell-model calculations. Two-body matrix elements are extracted from the data for the $(f_{5/2},g_{9/2})_{7^-}$ and $(g_{9/2})^2_{8^+}$ configurations.

I. INTRODUCTION

Spectroscopy of states with stretched two-nucleon configurations by appropriate transfer reactions reveals information on nuclear structure otherwise hardly accessible. In particular, the (α,d) reaction has been used as a valuable spectroscopic tool for the study of proton-neutron (pn) high-spin states over a wide range of nuclei (see, e.g., Ref. 1 and references therein). The similar kinematic properties of the $(\alpha, {}^2\mathrm{He})$ reaction have been utilized for investigations of neutron-neutron (nn) states coupled to maximum spin.[2–5] The selectivity of both reactions is due to the large negative Q values that kinematically favor rather large angular momentum transfers. In addition, the singlet state of the ^{2}He ejectile demands spin $S=0$ for the transferred nn pair. Thus, the reduced configuration space available leads to an enhanced selectivity of the $(\alpha, {}^2\mathrm{He})$ reaction compared to the (α,d) reaction where the pn pair is transferred in a relative triplet state ($S=1$).

Studies of the $(\alpha, {}^2\mathrm{He})$ reaction on p- and sd-shell nuclei have shown that states with a dominant $(d_{5/2})^2_{4^+}$ and $(d_{3/2},f_{7/2})_{5^-}$,$(f_{7/2})^2_{6^+}$ structure are preferentially populated.[3–5] Little information exists about nn high-spin states in the fp shell, because the analogous (t,p) reaction has not been investigated under similar kinematic conditions due to the lack of high energy ($E>60$ MeV) triton beams. Kinematically more suited light heavy-ion reactions suffer from structureless angular distributions and a difficult interpretation of the resulting spectra, which is caused by the simultaneous excitation of bound states in both ejectile and final nucleus.[6,7] For incident energies of about 56 MeV and fp shell targets, an angular momentum mismatch of $(6-8)\hbar$ is estimated for a surface reaction. From a comparison to the (α,d) reaction in the fp shell[8,9] it can be expected that transitions to nn configurations $(f_{5/2},g_{9/2})_{7^-}$, $(g_{9/2})^2_{8^+}$ and $(g_{9/2},d_{5/2})_{6^+}$ will be favored.

A very systematic behavior of the binding energies of nn high-spin states has been observed in the p and sd shell.[4] This is well reproduced by shell-model approaches, which are based on the assumption of pure two-nucleon states.[4,10] The present experiments extend the systematics to dominant transitions in the fp shell, and the applicability of the models mentioned above is investigated. Additionally, results of full shell-model calculations are shown, where binding energies and wave functions are obtained independently from the experimental information on the high-spin states and that permit a more rigorous test of the concept of pure configurations.

In the present study the $(\alpha, {}^2\mathrm{He})$ reaction is investigated on 18 targets ranging from ^{40}Ca to ^{72}Ge. Because of the small cross sections (typically 1–100 μb/sr) of the levels dominantly observed, a detection system is needed that offers both adequate efficiency for angular distribution measurements and good energy resolution.

Such a system was developed, and is described in Sec. II as well as the experimental procedure. The spins of preferentially populated transitions are deduced from a DWBA analysis of the experimental angular distributions. Details of the DWBA calculations are given in Sec. III. Section IV presents a discussion of the experimental results. In Sec. V, the systematics of the binding energies of experimentally identified high-spin states are compared with models that make use of their expected simple structure. The assumption of pure configurations is further tested in large scale shell-model calculations. A summary is given in Sec. VI.

II. EXPERIMENT

A. The ^{2}He detection system

The detection of the unbound reaction product ^{2}He is achieved by measuring the two breakup protons in coin-

cidence. The distribution of the relative energy ϵ between the outgoing protons has been the subject of several investigations[11,12] and shows a characteristic distribution peaking at $\epsilon \approx 500$ keV and decreases with a slope of approximately $1/\epsilon$ thereafter. This enhancement is attributed to the proton-proton (pp) final-state interaction of the unbound $^1S_0$ state of the ^{2}He system, which is usually described in the Watson-Migdal formalism.[13,14]

A transformation of the ^{2}He relative energy in its c.m. system to the laboratory system shows that all breakup protons are focused into a cone, as indicated by the velocity diagram in the upper part of Fig. 1. The maximum opening angle β_{max} is given by $\beta_{max} \simeq 2 \arctan\sqrt{\epsilon/E}$, where E denotes the ^{2}He laboratory energy. Additionally, the transformation leads to a concentration near the edge of the cone. In order to achieve an optimum efficiency it is important that the angular acceptance of the detection system covers the outskirts of this cone for typical ^{2}He laboratory energies. For example, assuming $\epsilon = 500$ keV and a ^{2}He laboratory energy range of $E = 30-50$ MeV this results in maximum opening angles of 11.4°–14.7°. These large acceptance angles are obtained by detecting the two protons in a pair of vertically arranged detector telescopes. The use of position-sensitive ΔE counters simultaneously permits large horizontal opening angles without deteriorating the energy resolution by kinematic broadening, which is essential for the purpose of the experiments. With this design an energy resolution of 200–300 keV full width at half maximum (FWHM) was achieved together with a reasonable efficiency (2–3 %).

The lower part of Fig. 1 shows a schematic diagram of the detection system. It consists of two identical large solid-angle counter telescopes collimated by 7.5 mm high and 12 mm wide slits, separated by an 8-mm high central post. At a distance of 8.6 cm to the target, this system subtends 15.2° vertical and 8° horizontal acceptance angles which results in a solid angle of 23 m sr for each telescope. Both telescopes consist of a 300-μm position-sensitive Si ΔE counter and a 5-mm Si(Li) E counter and enable the detection of protons between 6 and 31 MeV.

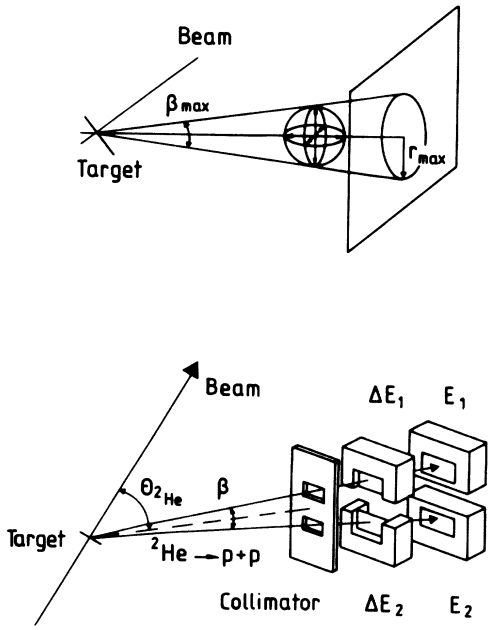

FIG. 1. Upper part: schematic velocity diagram for the detected protons. Lower part: schematic diagram of the detection system.

For the selection of ^{2}He events a fast coincidence is required between the two E counters, as the position-sensitive ΔE counters are not suitable for fast timing.[15] All energy and position signals were amplified using standard analog electronic circuitry. For each event, both $\Delta E, E$ and position ($\Delta E \cdot x$) signals together with the time-of-flight difference (ΔTOF) were transmitted to a VAX 11/750 computer and stored on magnetic tape. Time-of-flight differences up to 50 nsec were recorded to include random events for background analysis. A time resolution of 2–3 ns FWHM and a position resolution of 0.5 mm was typically achieved. Fast pileup rejection permitted high single-count rates (25000 s^{-1}) in each ΔE counter with an associated dead time of 25%. Stability and dead time of the electronic system were checked continuously with pulser signals, which were triggered by a monitor counter and fed into the preamplifiers.

B. Experimental procedure

The experiments were performed using ^{4}He beams from the Bonn isochroneous cyclotron. Table I lists the isotopic purities and thicknesses of the targets together with the beam energies. All targets were self supporting. The thicknesses were determined by normalizing the elastic cross sections to optical-model calculations at forward angles (see Sec. III). The total charge collected for each run was measured in a Faraday cup in order to determine absolute cross sections. The slightly different incident α energies were chosen to maintain optimum machine conditions for the high beam currents needed at larger detec-

TABLE I. Isotopic purities, target thicknesses, and bombarding energies.

Target	Isotopic purity (%)	Thickness (μg/cm^2)	E_α (MeV)
^{40}Ca	99.8	1110	55.7
^{42}Ca	87.7	530	55.7
^{44}Ca	97.8	840	55.3
^{48}Ca	97.0	880	55.3
^{50}Cr	96.8	270	55.4
^{52}Cr	99.9	650	55.8
^{54}Cr	93.6	390	55.8
^{54}Fe	99.7	260	55.6
^{56}Fe	99.7	140	55.6
^{58}Fe	93.2	810	55.7
^{58}Ni	99.8	200	55.6
^{60}Ni	99.1	240	55.6
^{62}Ni	97.7	450	57.2
^{64}Ni	93.7	130	55.6
^{64}Zn	99.4	330	56.1
^{66}Zn	99.0	270	56.0
^{70}Ge	92.4	260	55.6
^{72}Ge	98.2	360	55.6

tion angles. Beam intensities ranged from 70 nA at forward angles to 1 μA at backward angles, limited by the electronic dead time of the detection system. Typical acquisition times for one detector position were 8–16 h.

In the data analysis, protons were identified by two-dimensional windows on ΔE-E plots for both telescopes. After the selection of two-proton events, total energy and position signals were generated. The ^{2}He position information was used to calculate the kinematic correction of the energy signals, thereby revoking the kinematic broadening over the horizontal acceptance angle. Two electronic gates of equal width set on the ΔTOF spectrum to select coincidences resulting from one beam burst and random coincidences resulting from different beam bursts. The energy spectrum corresponding to random coincidences was used for background correction. For the resulting ^{2}He energy spectra an energy resolution of 200–300 keV was obtained leading to a $\pm$50 keV uncertainty in establishing the excitation energies of the observed peaks.

Typically, the (α,^{2}He) reaction was measured at four angles between 17.5° and 40° in order to kinematically identify states and extract angular distributions for significantly populated transitions. Furthermore, the position information was utilized to gain several data points for the angular distributions at each detector setting.

In order to determine the experimental ^{2}He cross sections the differential spectra $d^3\sigma/d\Omega_1 d\Omega_2 dE_1$ belonging to a specific state in the ^{2}He energy spectra were generated. The subscripts 1,2 denote the two detected protons. The continuous background was taken into account by linear interpolation for the region of interest. The spectra were then transformed into the c.m. system:

$$\frac{d^3\sigma}{d\Omega_{3-12} d\Omega_{12} d\epsilon} = \frac{1}{J(\epsilon)} \frac{d^3\sigma}{d\Omega_1 d\Omega_2 dE_1} \tag{1}$$

using the appropriate Jacobian for a three-particle reaction in the exit channel[16,17]

$$J(\epsilon) = \frac{m_1 m_2 m_3 p_1 p_2}{\mu_{12} p_{12} \mu_{3-12} p_{3-12} [m_2 + m_3 + (m_2/p_2^2)(\mathbf{p}_1 - \mathbf{P})\cdot\mathbf{p}_2]} . \tag{2}$$

Here, index 3 stands for the recoil nucleus, index 12 for the c.m. system of the two protons and index 3–12 for the overall c.m. system assuming a cluster structure of particles 1,2. Masses are denoted by m, momenta by p, and reduced masses by μ. $\mathbf{P}$ is the total momentum end ϵ is the relative pp energy. With the assumption of a ^{2}He cluster and a singlet state of the protons, the integration over Ω_{12} is straightforward and Ω_{3-12} is equal to the solid angle of the ^{2}He system. One gets

$$\frac{d\sigma}{d\Omega_{^2\mathrm{He,c.m.}}} = \tfrac{1}{2} 4\pi \int_{\epsilon_{\min}}^{\epsilon_{\max}} \frac{1}{J(\epsilon)} \frac{d^3\sigma}{d\Omega_1 d\Omega_2 dE_1} d\epsilon . \tag{3}$$

The factor $\frac{1}{2}$ results from the decay into identical particles. For more details of this calculation see Ref. 16.

Because of the integration over ϵ, it is important to choose consistent integration limits in order to obtain consistent results. The breakup energy was fixed to $\Delta\epsilon = 0.38$–1.07 MeV, which corresponds to the largest interval simultaneously observed for all analyzed transitions. However, the shape of the angular distributions is not affected by the integration limits, while the experimental cross sections are obviously sensitive to the choice of $\Delta\epsilon$. The resulting absolute differential cross sections are estimated to be accurate within $\pm$25%.

III. DWBA ANALYSIS

The angular distributions obtained for the (α,^{2}He) reaction were analyzed in the framework of the zero-range DWBA using the computer code DWUCK4.[18] A direct stripping process from the incident α particle was assumed where the neutron pair is transferred in a relative S state (spin $S=0$ and isospin $T=1$).

Optical potential parameters were extracted from an analysis of the simultaneously measured elastic α scattering. The computer code MAGALI[19] was used for the parameter search. For the description of the imaginary part only volume absorption was considered. The results of Ref. 20 for elastic α scattering on ^{58,60,62,64}Ni at $E_\alpha = 60$ MeV were used as start values for the search. Several equivalent (due to the Igo ambiguity[21]) parameter sets are offered in Ref. 20. In a more detailed analysis of the present results for the Ni isotopes, small differences in the description of the most backward angles were observed and the family giving the best results was chosen for all further calculations. Table II summarizes the best fit results for all investigated nuclei. Experimental and calculated angular distributions are displayed in Fig. 2. A satisfactory reproduction of the experimental angular distributions can be stated for all target nuclei investigated.

An averaged mass-, charge-, and energy-dependent potential parameter set for elastic deuteron scattering (Ref. 22, set I) was selected to describe the outgoing channels. The spin-orbit term was neglected, since $S=0$ was assumed for the ^{2}He ejectile. This potential permits a good description over a wide mass range and for typical ^{2}He energies of the present experiment. For completeness, the deuteron parameters are given in Table III.

Bound state wave functions were calculated in a Woods-Saxon potential with a radius $r=1.25$ fm, a diffuseness of $a=0.65$ fm and a spin-orbit coupling of $V_{LS}=6$ MeV. The depths of the potential wells were adjusted to reproduce the binding energies of the corresponding single particle states. The relevant single particle energies were taken from investigations of the (d,p) reaction for all target nuclei (see Ref. 23 and references therein). The two-nucleon microscopic form factors were generated by DWUCK4 following the method of Bayman and Kallio.[24] Only pure nn configurations were considered. The results for a given nn configuration are related to the experimental cross section by

TABLE II. Optical potential parameters for the incoming channel (target+α) used in the DWBA analysis.

Target	V (MeV)	r_v (fm)	a_v (fm)	W (MeV)	r_w (fm)	a_w (fm)	r_c (fm)
^{40}Ca	230.1	1.26	0.67	23.8	1.50	0.79	1.3
^{42}Ca	222.8	1.26	0.68	30.0	1.50	0.62	1.3
^{44}Ca	226.9	1.26	0.70	20.0	1.69	0.49	1.3
^{48}Ca	223.1	1.26	0.69	26.1	1.50	0.62	1.3
^{50}Cr	226.0	1.26	0.70	29.7	1.62	0.49	1.3
^{52}Cr	220.8	1.26	0.69	19.7	1.58	0.60	1.3
^{54}Cr	220.0	1.26	0.68	20.0	1.58	0.65	1.3
^{54}Fe	208.3	1.26	0.70	18.2	1.60	0.51	1.3
^{56}Fe	207.4	1.26	0.69	18.4	1.60	0.56	1.3
^{58}Fe	209.0	1.26	0.70	22.1	1.60	0.60	1.3
^{58}Ni	226.0	1.26	0.69	24.1	1.57	0.50	1.3
^{60}Ni	225.1	1.26	0.67	21.6	1.59	0.51	1.3
^{62}Ni	229.1	1.26	0.61	31.1	1.41	0.67	1.3
^{64}Ni	213.5	1.26	0.66	32.6	1.44	0.63	1.3
^{64}Zn	217.1	1.26	0.71	20.3	1.60	0.59	1.3
^{66}Zn	217.3	1.26	0.67	22.9	1.60	0.54	1.3
^{70}Ge	228.4	1.26	0.72	20.7	1.60	0.65	1.3
^{72}Ge	222.1	1.26	0.67	26.6	1.60	0.59	1.3

$$\frac{d\sigma}{d\Omega_{\text{expt}}} = N(\Delta\epsilon)\frac{d\sigma}{d\Omega_{\text{DW}}} , \tag{4}$$

where N denotes an overall normalization constant. For a fixed breakup energy interval $\Delta\epsilon$ this normalization should be independent of the incident energy and the particular structure of the target nucleus.

Since only even-even target nuclei were investigated, all ground state (g.s.) transitions have a $L=0$ transfer. The angular distributions (Fig. 3) show a pronounced oscillatory behavior and permit a sensitive test of the selected optical potential parameters. A modification of the potential was found necessary in order to reproduce the experimental g.s. angular distributions with correct phase. In all calculations the depth of the real potential for the outgoing channel was increased by 10 MeV compared to the value given in Ref. 22. The need for this correction stems from the energy dependence of the optical potential. Because of its higher charge, the ^{2}He possesses a smaller effective scattering energy for identical kinetic energies than does the deuteron. The nonlocality of the optical potential leads to an increase of the potential depth for decreasing scattering energies.

TABLE III. Optical-potential parameters for the outgoing channel (final nucleus+^{2}He) used in the DWBA analysis. The parameters are calculated for every final state as a function of charge Z, mass number A, and laboratory energy $E_{^2\text{He}}$.

Parameter	Function
V (MeV)	$89+1.5(Z/A^{1/3})-E_{^2\text{He}}$
r_v (fm)	1.25
a_v (fm)	$0.81-0.023A^{1/3}$
W (MeV)	13
r_w (fm)	1.25
a_w (fm)	$0.51+0.075A^{1/3}$
r_c (fm)	1.3

The resulting DWBA calculations for the g.s. transitions are summarized in Fig. 3. A good description of the experimental angular distributions is found over the entire mass range investigated. In order to retain a consistent description which allows a comparison between results for different configurations or target nuclei, no other attempt was made to modify the DWBA calculations.

IV. RESULTS AND DISCUSSION

In preceding investigations[2–4] of the (α,^{2}He) reaction on p- and sd-shell nuclei, a pronounced selectivity for kinematically favored transitions to stretched configurations was observed. At bombarding energies of 56 MeV, the angular momentum mismatch is estimated to be about $(6-8)\hbar$ for a surface reaction and fp shell target nuclei. Therefore, a preferential population of states formed by capturing the two neutrons coupled to fully stretched $(f_{5/2},g_{9/2})_{7^-}$, $(g_{9/2})^2_{8^+}$ and $(g_{9/2},d_{5/2})_{6^+}$ configurations is expected.

The results presented in this section are divided into two parts. In Sec. IV A the (α,^{2}He) reaction on Fe, Ni, Zn, and Ge targets will be discussed. It shows optimum conditions for the excitation of the nn configurations indicated above. Results for the Cr and Ca targets will be presented in Sec. IV B, ordered by decreasing mass number as the experimental difficulties to identify the 7^-, 8^+, and 6^+ states increase correspondingly: The angular momentum mismatch is slightly lowered and the opening of the $f_{7/2}$ shell increases the number of possible stretched two-nucleon states considerably. Furthermore, the relevant single-particle strengths tend to be more and more fragmented.

A typical energy spectrum of the (α,^{2}He) reaction is shown for each target, followed by angular distributions

of the differential cross sections for the most prominent levels. Error bars on the experimental points represent statistical errors only. DWBA calculations are shown as solid, dashed, and dashed-dotted lines. The curves are normalized to fit the data. Although calculations were performed for all reasonable L transfers, in most cases only results for the most probable L value are shown for clarity. Excitation energies and DWBA calculations are summarized in a table for each final nucleus.

A knowledge of the transferred angular momentum establishes the J^{π} value of the final state, because the selec-

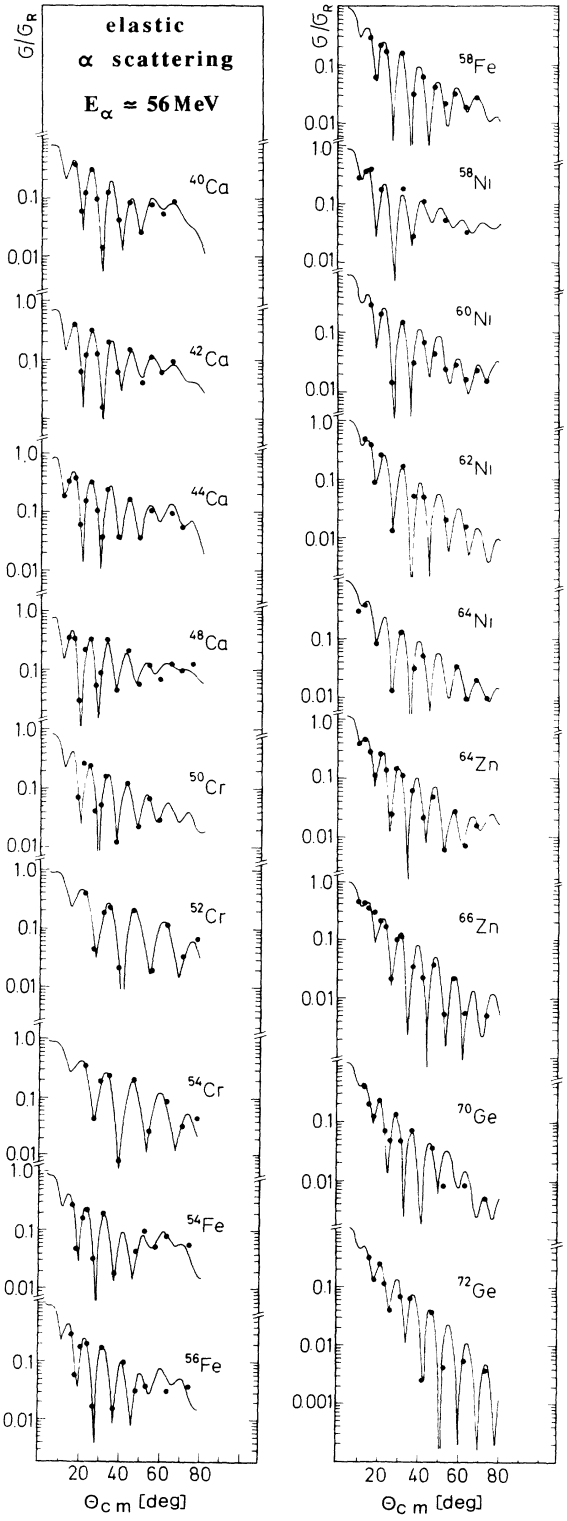

FIG. 2. Angular distributions of elastic α scattering on ^{40,42,44,48}Ca, ^{50,52,54}Cr, ^{54,56,58}Fe, ^{58,60,62,64}Ni, ^{64,66}Zn, and ^{70,72}Ge. The optical-model fits are calculated with the parameters given in Table II.

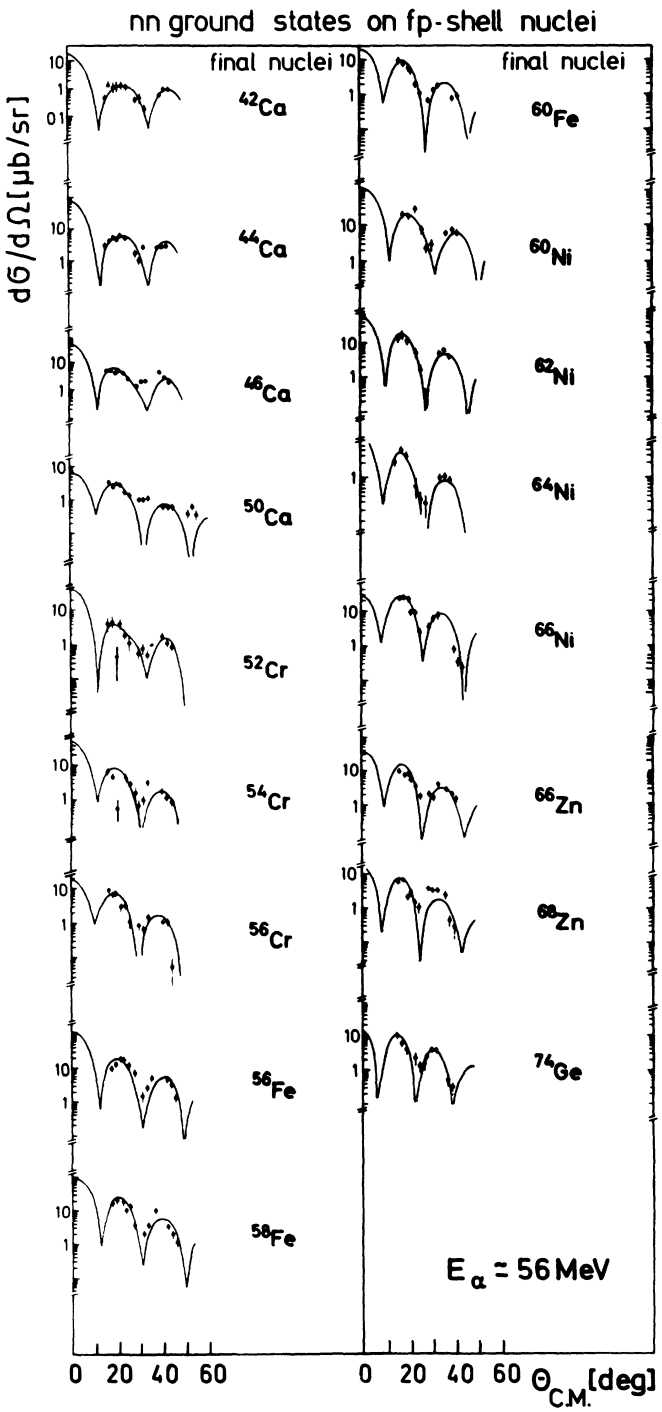

FIG. 3. Ground-state angular distributions of the $(\alpha,{}^2\mathrm{He})$ reaction on ^{40,42,44,48}Ca, ^{50,52,54}Cr, ^{54,56,58}Fe, ^{58,60,62,64}Ni, ^{64,66}Zn, and ^{70,72}Ge. The DWBA calculations (solid lines) are described in the text.

tion rules ($\Delta S=0, \Delta T=1$) permit the excitation of natural parity states only. For a given L value, the shapes of the calculated angular distributions are fairly insensitive to the total reaction Q value and the single-particle states taken into account. Thus, L transfers not shown for a certain state can be procured from the DWBA calculations for other levels.

While the assumption of a constant DWBA normalization of the $(\alpha,{}^2\mathrm{He})$ reaction depends on the validity of the simple picture of pure configurations employed, a consistent description of the transition strengths to states in a given final nucleus can be expected. The normalization depends strongly on the binding energies of the single-particle states and in some cases allows a distinction between different nn configurations coupled to the same J^π. Only configurations coupled to maximum spin are considered, since couplings not fully stretched like $(g_{9/2})^2_{6^+}$, $(f_{5/2},g_{9/2})_{5^-}$ lead to DWBA cross sections that are roughly an order of magnitude smaller than results for stretched configurations.

Compared to the high-spin states, very large normalization values occur for most g.s. transitions. This can be attributed to the neglection of configuration mixing.

Results from other investigations of α-induced two-nucleon transfer indicate that the differences of the excitation energies of stretched configurations roughly reflect the energy spacing of the corresponding single-particle states.[10] This behavior provides additional information for the interpretation of the observed spectra.

A. Fe, Ni, Zn, and Ge targets

1. $^{54}Fe(\alpha,{}^2He)^{56}Fe$

As an example, the reaction $^{54}\mathrm{Fe}(\alpha,{}^2\mathrm{He})^{56}\mathrm{Fe}$ will be discussed in more detail to give an impression on the quality of the proposed J^π and configuration assignments.

A spectrum of this reaction is shown in Fig. 4. It is dominated by five strongly populated states, which demonstrates the selectivity of the $(\alpha,{}^2\mathrm{He})$ reaction. Angular distributions and DWBA calculations for these levels together with the state at 3.10 MeV and the g.s. transition are depicted in Fig. 5. The well-known[23] first- and second-excited state in ^{56}Fe with $J^\pi=2^+$ and 4^+, respectively, correspond to the weakly populated 0.84-MeV and 2.02-MeV levels. The peak at 4.41 MeV shows large variations in the angular distribution, eventually due to an unresolved doublet structure. Therefore, no DWBA calculations were performed for this level. A summary of the obtained excitation energies and the results of the DWBA calculations for the $^{54}\mathrm{Fe}(\alpha,{}^2\mathrm{He})^{56}\mathrm{Fe}$ reaction is given in Table IV.

The g.s. transition is described reasonably well as discussed in Sec. III. The 3.10-MeV level is best reproduced by $J^\pi=4^+$ in accordance with results from an investigation of the $^{54}\mathrm{Fe}(\alpha,pp\gamma)^{56}\mathrm{Fe}$ reaction.[25] The assumption of a $(p_{3/2},f_{5/2})_{4^+}$ configuration results in a reasonable normalization compared to the high-spin states. Regard-

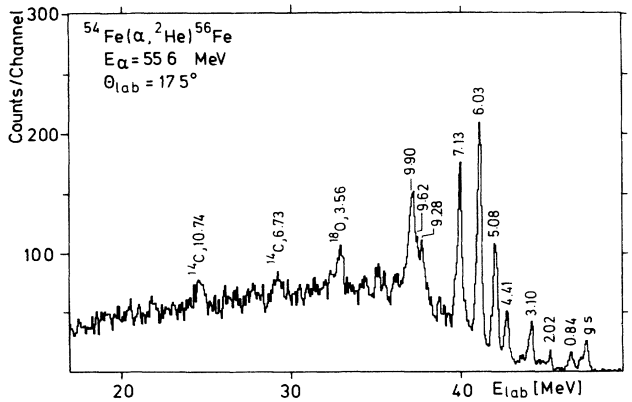

FIG. 4. Spectrum of the $^{54}\mathrm{Fe}(\alpha,{}^2\mathrm{He})^{56}\mathrm{Fe}$ reaction at $E_\alpha=55.6$ MeV and $\theta_{\mathrm{lab}}=17.5°$.

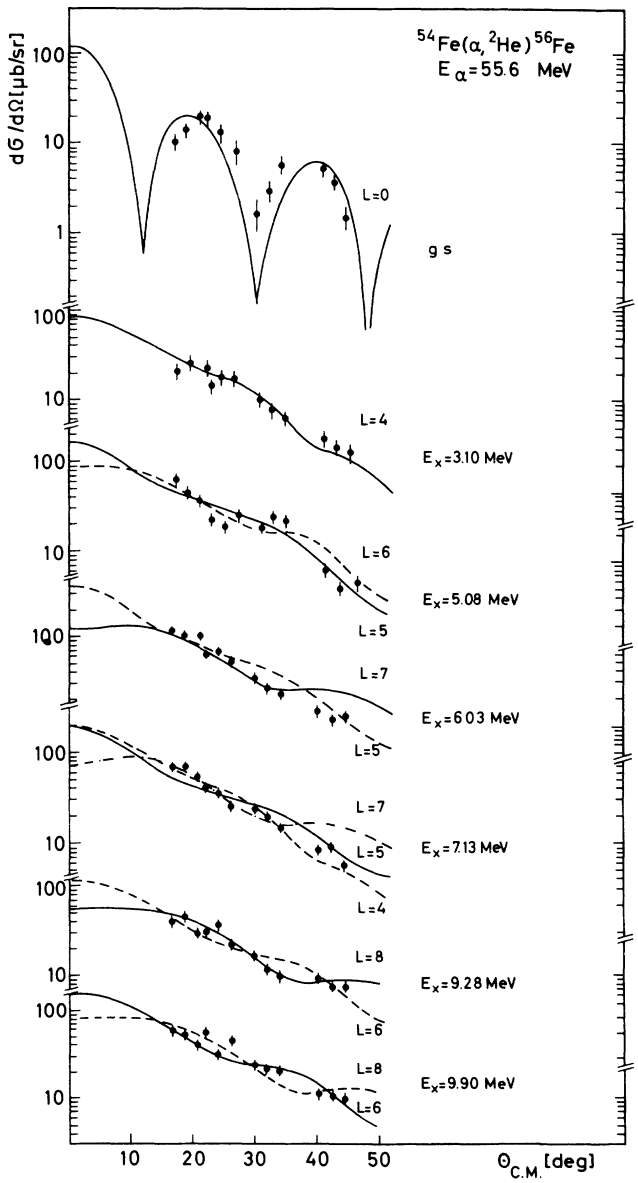

FIG. 5. Angular distributions of transitions to states populated in the $^{54}\mathrm{Fe}(\alpha,{}^2\mathrm{He})^{56}\mathrm{Fe}$ reaction. The curves are DWBA calculations. See text.

TABLE IV. DWBA calculations for prominent transitions of the $^{54}Fe(\alpha,^2He)^{56}Fe$ reaction and comparison to other work.

E_x (MeV)	J^π	$(\alpha,^2He)$ nn configuration	N	Other work[a] E_x (MeV)	J^π
g.s.	0^+	$(p_{3/2})^2_{0^+}$	600±250		
3.10	4^+	$(p_{3/2},f_{5/2})_{4^+}$	180±35	3.12	4^+
5.08	5^-	$(p_{1/2},g_{9/2})_{5^-}$	130±40		
	5^-	$(p_{3/2},g_{9/2})_{5^-}$	95±30		
	5^-	$(f_{5/2},d_{5/2})_{5^-}$	40±10		
	6^+	$(g_{9/2},d_{5/2})_{6^+}$	50±15		
6.03	7^-	$(f_{5/2},g_{9/2})_{7^-}$	110±40		
	5^-	$(f_{5/2},d_{5/2})_{5^-}$	180±50		
7.13	5^-	$(f_{5/2},d_{5/2})_{5^-}$	125±25		
	7^-	$(f_{5/2},g_{9/2})_{7^-}$	90±30		
	4^+	$(p_{3/2},f_{5/2})_{4^+}$	450±150		
9.28	8^+	$(g_{9/2})^2_{8^+}$	190±40		
	6^+	$(g_{9/2},d_{5/2})_{6^+}$	100±30		
9.90	6^+	$(g_{9/2},d_{5/2})_{6^+}$	180±40		
	8^+	$(g_{9/2})^2_{8^+}$	350±80		

[a]Reference 25.

ing the 5.08-MeV state, an $L=5$ transition is slightly preferred in comparison to $L=6$, but no clear distinction can be made. From the possible configurations, $(g_{9/2},d_{5/2})_{6^+}$ and $(f_{5/2},d_{5/2})_{5^-}$ are strongly overpredicted in the calculations. The assumption of a $(p_{1/2},g_{9/2})_{5^-}$ configuration leads to a normalization consistent with the values given for other states. Therefore, a tentative 5^- assignment is given. However, the $(p_{1/2},g_{9/2})_{5^-}$ configuration cannot be discriminated clearly from a $(p_{3/2},g_{9/2})_{5^-}$ coupling. The predicted cross section for the latter case is smaller by a factor 0.7, which is still within the range of the values given in Table IV. This normalization ratio is typical for all calculations of these two configurations in other final nuclei and in the following subsections the discussion will be restricted to the $(p_{1/2},g_{9/2})_{5^-}$ configuration only.

The states at 6.03 and 7.13 MeV correspond most likely to the $(f_{5/2},g_{9/2})_{7^-}$ and $(f_{5/2},d_{5/2})_{5^-}$ configurations, respectively. Although the angular pattern can be reproduced reasonably well by other L values (e.g., $L=4$ for 7.13 MeV) the normalization constants for all other couplings are very small. For all reactions discussed in this subsection the DWBA calculations predict the largest cross sections for a $(f_{5/2},g_{9/2})_{7^-}$ configuration which supports the 7^- assignment for the state at 6.03 MeV.

The two states observed at higher excitation energies most likely correspond to the $(g_{9/2})^2_{8^+}$ and $(g_{9/2},d_{5/2})_{6^+}$ configurations, respectively. The large energy gap between the relevant f,p and g,d single-particle states favors this interpretation. The assignments $L=8$, $E_x=9.28$ MeV and $L=6$, $E_x=9.90$ MeV follow from the better reproduction of the angular distributions as well as the large difference in the normalization constants considering the reverse case. It should be mentioned that the unfolding of the small peak at 9.62 MeV from the 9.90-MeV level causes an additional 10% uncertainty in the experimental ^2He cross section, but hardly affects the shape of the angular distribution.

2. $^{56}Fe(\alpha,^2He)^{58}Fe$

A spectrum of the reaction and angular distributions of the transitions to the prominent levels are given in Figs. 6 and 7, respectively. The largest peak exhibits an unresolved doublet structure with a dominant level at 4.61 MeV and a smaller one at 4.84 MeV. The DWBA calculation strongly favors an $L=7$ transition for the 4.61-MeV state. The best reproduction of the angular distribution is obtained assuming an $L=7+L=5$ doublet. From the normalization constant a $(f_{5/2},g_{9/2})_{7^-}+(p_{1/2},g_{9/2})_{5^-}$ configuration is likely. The 4.84-MeV state agrees with the observation of a level at 4.81 MeV and a proposed $L=5,6$ assignment[26] in the nn transfer reaction $^{56}Fe(t,p)^{58}Fe$.

A $L=5$ assignment with a $(f_{5/2},d_{5/2})_{5^-}$ configuration

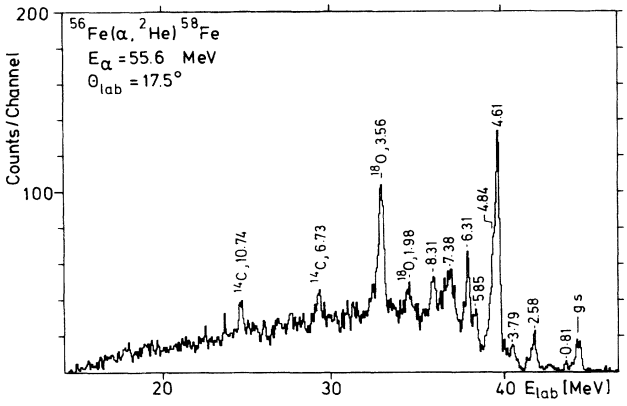

FIG. 6. Spectrum of the ^{56}Fe(α,^{2}He)^{58}Fe reaction at $E_\alpha = 55.6$ MeV and $\theta_{lab} = 17.5°$.

for the 6.31-MeV state is suggested from the good reproduction of shape and relative strength of the angular distribution. Again, a clear distinction between the $L = 8$ and $L = 6$ transition can be accomplished by comparing the DWBA calculations. An assignment $E_x = 7.38$ MeV, $(g_{9/2})^2_{8^+}$ and $E_x = 8.31$ MeV, $(g_{9/2},d_{5/2})_{6^+}$ is clearly favored. A summary of the DWBA results is given in Table V.

3. ^{58}Fe(α,^{2}He)^{60}Fe

Figure 8 shows a spectrum of this reaction at $\theta_{lab} = 17.5°$. Angular distributions for all observed states are given in Fig. 9. The two moderately populated levels at 3.08 and 3.52 MeV are tentatively assigned $L = 4$,

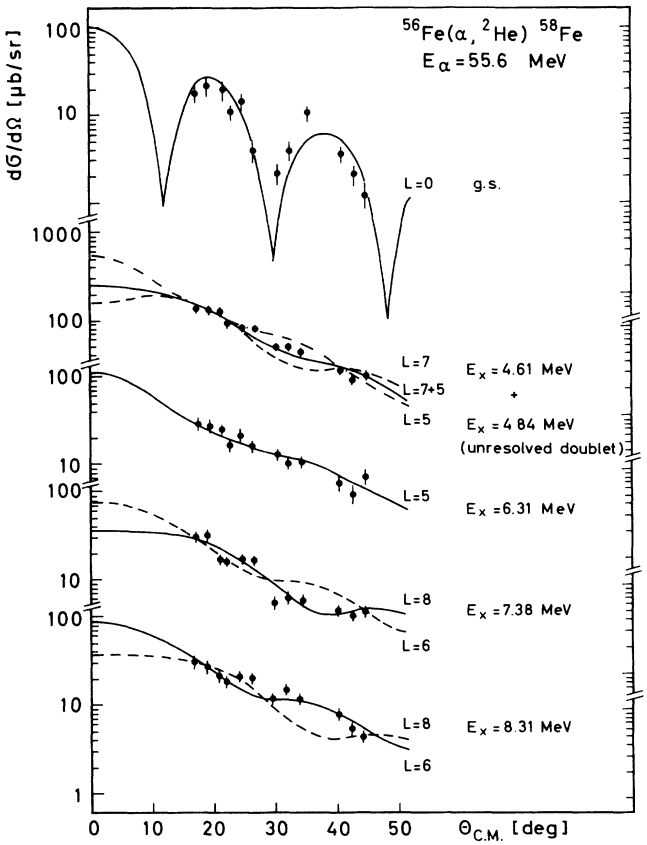

FIG. 7. Angular distributions of transitions to states populated in the ^{56}Fe(α,^{2}He)^{58}Fe reaction. The curves are DWBA calculations. See text.

TABLE V. DWBA calculations for prominent transitions of the ^{56}Fe(α,^{2}He)^{58}Fe reaction and comparison to other work.

				Other work[a]	
E_x (MeV)	J^π	(α,^{2}He) *nn* configuration	N	E_x (MeV)	J^π
g.s.	0^+	$(p_{1/2})^2_{0^+}$	1600±700		
4.65[b]	7^-	$(f_{5/2},g_{9/2})_{7^-}$		4.81	$(5^-,6^+)$
	+	+	160±35[c]		
	5^-	$(p_{1/2},g_{9/2})_{5^-}$			
	7^-	$(f_{5/2},g_{9/2})_{7^-}$	225±60		
	5^-	$(p_{1/2},g_{9/2})_{5^-}$	600±190		
6.31	5^-	$(f_{5/2},d_{5/2})_{5^-}$	120±25		
7.38	8^+	$(g_{9/2})^2_{8^+}$	150±35		
	6^+	$(g_{9/2},d_{5/2})_{6^+}$	95±30		
8.31	6^+	$(g_{9/2},d_{5/2})_{6^+}$	150±35		
	8^+	$(g_{9/2})^2_{8^+}$	260±90		

[a]Reference 30.
[b]Unresolved doublet at 4.61 and 4.84 MeV.
[c]DWBA calculation for a $(f_{5/2},g_{9/2})_{7^-}+(p_{1/2},g_{9/2})_{5^-}$ doublet.

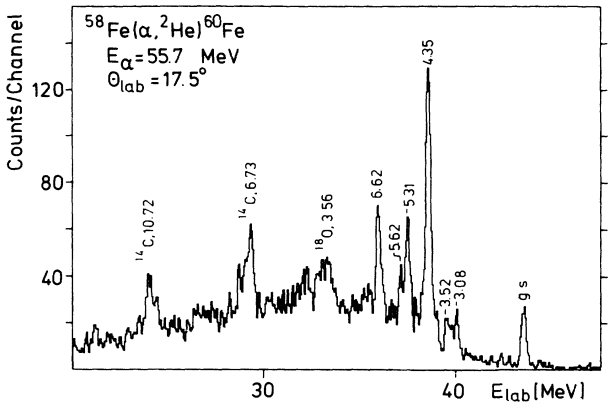

FIG. 8. Spectrum of the $^{58}\mathrm{Fe}(\alpha,{}^2\mathrm{He})^{60}\mathrm{Fe}$ reaction at $E_\alpha=55.7$ MeV and $\theta_{\mathrm{lab}}=17.5°$.

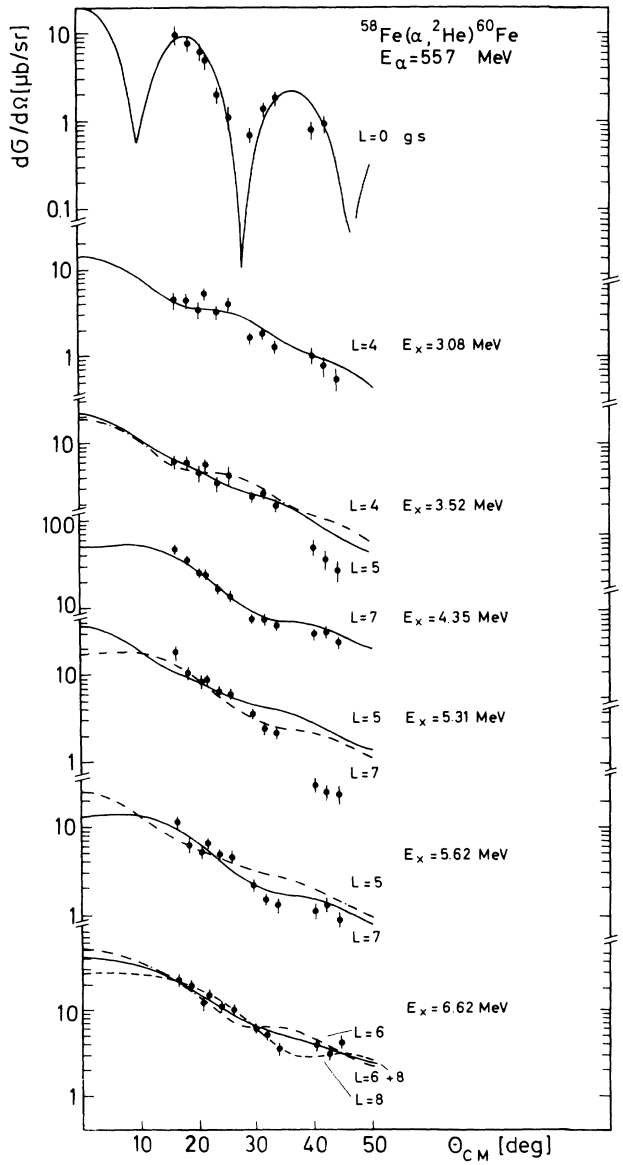

FIG. 9. Angular distributions of transitions to states populated in the $^{58}\mathrm{Fe}(\alpha,{}^2\mathrm{He})^{60}\mathrm{Fe}$ reaction. The curves are DWBA calculations. See text.

which is supported by the relative strength and, for the 3.08-MeV state, by the reproduction of the angular distribution. Regarding the shape of the angular distributions two $L=7$ assignments are favored. The far most prominent state at 4.35 MeV is attributed to a $(f_{5/2},g_{9/2})_{7^-}$ transition which results in a reasonable normalization constant. The origin of the second $L=7$ transition at 5.62 MeV is unclear. It might arise from a splitting of the $f_{5/2}$ single-particle strength observed[27] in ^{59}Fe, where two dominant $\frac{5}{2}^-$ states with an energy difference of 1.1 MeV and a cross-section ratio of $\approx$4:1 have been found. This coincides roughly with the proportion of the experimental cross sections.

The experimental angular distribution of the rather prominent 5.31-MeV level shows a large deviation at the most backward detector position in comparison to all performed DWBA computations. Since the number of neutrons is the same for the target nucleus ^{60}Ni and the spectrum of the $^{60}\mathrm{Ni}(\alpha,{}^2\mathrm{He})^{62}\mathrm{Ni}$ reaction (discussed in Sec. IV A 5) exhibits a very similar structure, a $(f_{5/2},d_{5/2})_{5^-}$ configuration would be favored by the comparison, resulting in a normalization constant at forward angles well within the frame of typical values for the $^{58}\mathrm{Fe}(\alpha,{}^2\mathrm{He})^{60}\mathrm{Fe}$ reaction. The peak at 6.62 MeV is tentatively assigned to be an unresolved $(g_{9/2})^2_{8^+}$ $+(g_{9/2},d_{5/2})_{6^+}$ doublet. From the quality of the data, a pure $L=6$ state with configuration $(g_{9/2},d_{5/2})_{6^+}$ cannot be excluded. The summed DWBA angular distribution permits a somewhat better reproduction of the experimental data and the corresponding normalization constant agrees very closely with the value for the 7^- transition. In addition, the excitation energies of the $g_{9/2}$ and $d_{5/2}$ single-particle states are almost identical. Table VI presents an overview of the DWBA results.

4. $^{58}Ni(\alpha,{}^2He)^{60}Ni$

A spectrum of this reaction at $\theta_{\mathrm{lab}}=17.5°$ and the extracted angular distributions are displayed in Figs. 10 and 11, respectively. Two comparable experiments have been performed on the target nucleus ^{58}Ni, namely a study of the $(\alpha,{}^2\mathrm{He})$ reaction at 65 MeV incident energy[5] and an investigation of the $(\alpha,pp\gamma)$ reaction.[28] The results of Ref. 5 show systematically larger excitation energies for the preferentially populated transitions, the differences varying from $\approx$200 keV between 5–7 MeV to $\approx$400 keV at 9–10 MeV. On the other hand, the excitation energies obtained in the present experiment, which are summarized in Table VII, agree within the quoted errors with those states observed in the $(\alpha,pp\gamma)$ reaction.

The DWBA calculations are in agreement with the g.s. and the well-established[23] $J^\pi=4^+$ character of the 2.51-MeV state. The dominant peak at 5.31 MeV contains a contribution of a weakly excited level at 5.00 MeV. The doublet structure can be seen more clearly at backward angles (not shown) due to the different steepness of the corresponding angular distributions. An $L=7$ assumption well describes the experimental curve. The addition of the $L=5$ calculation hardly affects the shape but lowers the normalization to a value that corresponds

TABLE VI. DWBA calculations for prominent transitions of the ^{58}Fe(α,^{2}He)^{60}Fe reaction.

E_x (MeV)	J^π	nn configuration	N
g.s.	0^+	$(p_{3/2})^2_{0+}$	260±100
3.08	4^+	$(p_{3/2},f_{5/2})_{4+}$	60±20
3.52	4^+	$(p_{3/2},f_{5/2})_{4+}$	60±30
	5^-	$(p_{1/2},g_{9/2})_{5-}$	40±20
4.35	7^-	$(f_{5/2},g_{9/2})_{7-}$	70±10
5.31	5^-	$(f_{5/2},d_{5/2})_{5-}$	60±20
	7^-	$(f_{5/2},g_{9/2})_{7-}$	30±15
5.62	7^-	$(f_{5/2},g_{9/2})_{7-}$	20±5
	5^-	$(f_{5/2},d_{5/2})_{5-}$	40±10
6.62	8^+	$(g_{9/2})^2_{8+}$	
	+	+	70±20[a]
	6^+	$(g_{9/2},d_{5/2})_{6+}$	
	6^+	$(g_{9/2},d_{5/2})_{6+}$	120±30
	8^+	$(g_{9/2})^2_{8+}$	200±120

[a]DWBA calculation for a $(g_{9/2})^2_{8+}+(g_{9/2},d_{5/2})_{6+}$ doublet.

better to the other results. The investigation of the $(\alpha,pp\gamma)$ reaction[28] reveals corresponding states $J^\pi=7^-$, $E_x=5.35$ MeV and $J^\pi=5^-$, $E_x=5.01$ MeV with proposed nn configurations $(f_{5/2},g_{9/2})_{7-}$ and $(p_{1/2},g_{9/2})_{5-}$, respectively, which strengthens the confidence of the assignments given in the present study.

Assuming a $(f_{5/2},d_{5/2})_{5-}$ configuration, a good correspondence is found for the 6.56-MeV state both in magnitude and shape. The states at 8.76 and 9.31 MeV are described best by an $L=6$ transfer. The normalization constant for a $(g_{9/2},d_{5/2})_{6+}$ configuration is reasonable for the 9.31-MeV level, but too small for the 8.76-MeV state. The normalization obtained for a $(g_{9/2})^2_{8+}$ configuration plus the resemblance to the ^{56}Fe(α,^{2}He)^{58}Fe spectrum, due to the identical neutron number, leads to a preference of $L=8$ for the latter state.

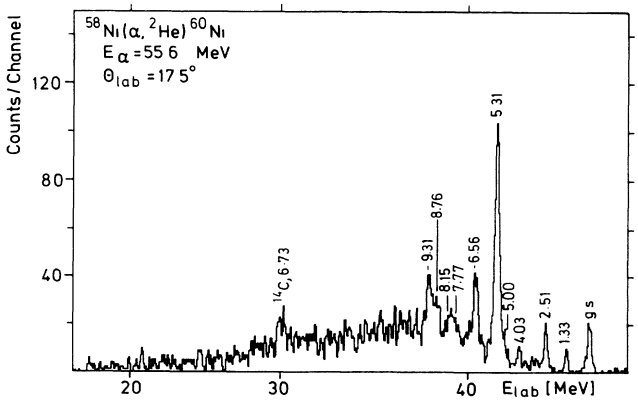

FIG. 10. Spectrum of the ^{58}Ni(α,^{2}He)^{60}Ni reaction at $E_\alpha=55.6$ MeV and $\theta_{lab}=17.5°$.

5. ^{60}Ni(α,^{2}He)^{62}Ni

Figure 12 displays a spectrum of this reaction at $\theta_{lab}=17.5°$. The analyzed angular distributions are displayed in Fig. 13, and the corresponding DWBA calculations are given in Table VIII. Various weak transitions are visible below 5 MeV excitation energy. The statistics restricted an extraction of angular distributions to the levels at 4.11 and 4.98 MeV. Both states are described well by an $L=4$ transition. The complexity of the low-energy spectrum and the large normalization constants for possible nn configurations [e.g., $(p_{3/2},f_{5/2})_{4+}$ compared to the high-spin states discussed below imply a considerable degree of configuration mixing for these states.

The dominant peak at 4.63 MeV is expected to have a $(f_{5/2},g_{9/2})_{7-}$ configuration that is clearly supported by

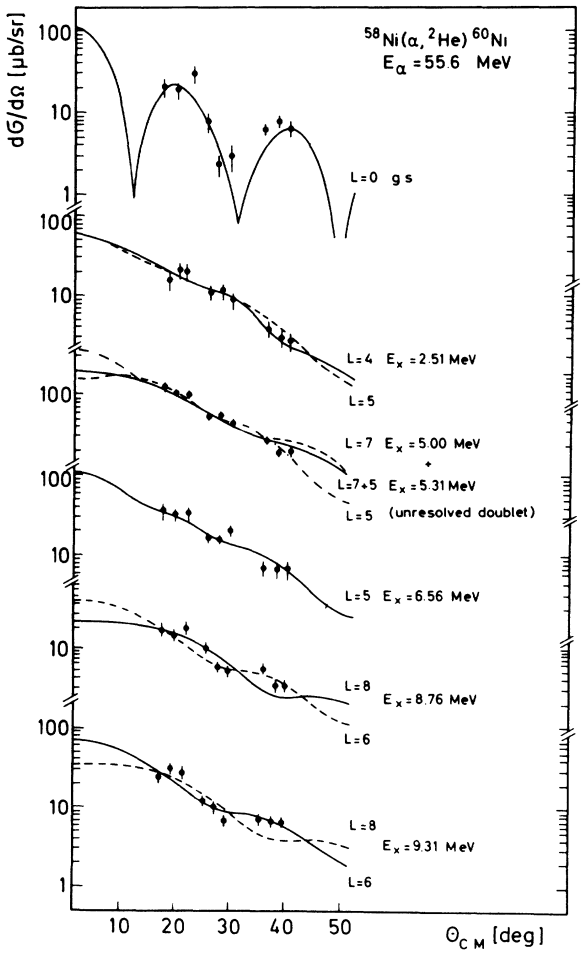

FIG. 11. Angular distributions of transitions to states populated in the ^{58}Ni(α,^{2}He)^{60}Ni reaction. The curves are DWBA calculations. See text.

TABLE VII. DWBA calculations for prominent transitions of the $^{58}Ni(\alpha,^2He)^{60}Ni$ reaction and comparison to other work.

				Other work[a]	
E_x (MeV)	J^π	$(\alpha,^2He)$ *nn* configuration	N	E_x (MeV)	J^π
g.s.	0^+	$(p_{3/2})^2_{0^+}$	590±250		
2.51	4^+	$(p_{3/2},f_{5/2})_{4^+}$	130±25	2.51	4^+
5.27[b]	5^-	$(p_{1/2},g_{9/2})_{5^-}$		5.01	5^-
	+	+	130±25[c]		
	7^-	$(f_{5/2},g_{9/2})_{7^-}$		5.35	7^-
	7^-	$(f_{5/2},g_{9/2})_{7^-}$	190±40		
	5^-	$(p_{1/2},g_{9/2})_{5^-}$	440±80		
6.56	5^-	$(f_{5/2},d_{5/2})_{5^-}$	110±20		
8.76	8^+	$(g_{9/2})^2_{8^+}$	125±40		
	6^+	$(g_{9/2},d_{5/2})_{6^+}$	60±15		
9.31	6^+	$(g_{9/2},d_{5/2})_{6^+}$	90±20		
	8^+	$(g_{9/2})^2_{8^+}$	190±50		

[a]Reference 28.
[b]Unresolved doublet at 5.00 and 5.31 MeV.
[c]DWBA calculation for a $(f_{5/2},g_{9/2})_{7^-}+(p_{1/2},g_{9/2})_{5^-}$ doublet.

the DWBA calculation. A tentative $(f_{5/2},d_{5/2})_{5^-}$ assignment is given for the 5.66-MeV state, mainly based on the relative magnitude of the DWBA calculation that predicts the second largest cross section for a $(f_{5/2},d_{5/2})_{5^-}$ coupling. The experimental angular distribution of the 6.06-MeV peak supports $L>4$, but no definite conclusion can be drawn because the enlarged line width indicates a doublet.

Taking into account the energies of the single-particle states in ^{61}Ni, $L=8$ and $L=6$ are expected for the states at 7.19 and 7.62 MeV. The width of the 7.19-MeV state is again broadened due to a contribution from a weaker state. The angular distributions do not allow to distinguish between $L=8$ and $L=6$, but the normalization relative to the 7^- state and the spacing of the lowest $g_{9/2}$ and $d_{5/2}$ state in ^{61}Ni favor $E_x=7.19$ MeV, $(g_{9/2})^2_{8^+}$ and $E_x=7.62$ MeV, $(g_{9/2},d_{5/2})_{6^+}$.

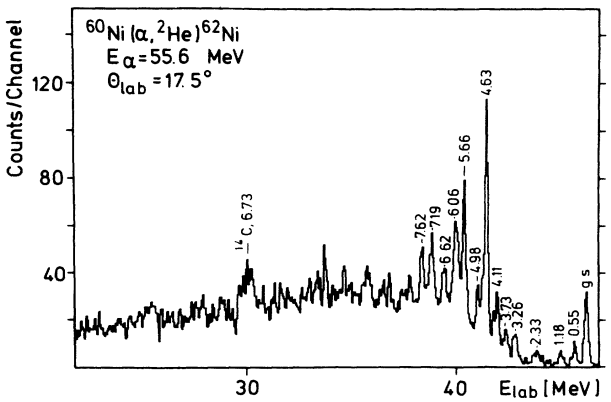

FIG. 12. Spectrum of the $^{60}Ni(\alpha,^2He)^{62}Ni$ reaction at $E_\alpha=55.6$ MeV and $\theta_{lab}=17.5°$.

6. $^{62}Ni(\alpha,^2He)^{64}Ni$

A spectrum of this reaction, given in Fig. 14, displays the extreme selectivity of the $(\alpha,^2He)$ reaction. Only

TABLE VIII. DWBA calculations for prominent transitions of the $^{60}Ni(\alpha,^2He)^{62}Ni$ reaction.

E_x (MeV)	J^π	*nn* configuration	N
g.s.	0^+	$(p_{3/2})^2_{0^+}$	340±100
4.11	4^+	$(p_{3/2},f_{5/2})_{4^+}$	90±15
4.63	7^-	$(f_{5/2},g_{9/2})_{7^-}$	50±10
4.98	4^+	$(p_{3/2},f_{5/2})_{4^+}$	85±10
5.66	5^-	$(f_{5/2},d_{5/2})_{5^-}$	75±15
6.06[a]	5^-	$(f_{5/2},d_{5/2})_{5^-}$	70±15
	7^-	$(f_{5/2},g_{9/2})_{7^-}$	60±15
7.19[a]	8^+	$(g_{9/2})^2_{8^+}$	130±25
	6^+	$(g_{9/2},d_{5/2})_{6^+}$	65±15
7.62	6^+	$(g_{9/2},d_{5/2})_{6^+}$	55±25
	8^+	$(g_{9/2})^2_{8^+}$	100±40

[a]Unresolved doublet.

three states are excited with large cross sections that are expected from Q-value systematics and simple shell-model considerations to correspond to the 7^-, 8^+, and 6^+ transitions (see Sec. V). The angular distributions are presented in Fig. 15 and a summary of DWBA results is given in Table IX.

The most prominent transition at 4.60 MeV is assigned $(f_{5/2},g_{9/2})_{7^-}$, justified by the reproduction of the shape and the relative strength in the DWBA calculation. The unfolding of the 5.81-MeV, 6.03-MeV doublet introduces some additional uncertainty in distinguishing the $L=6$ and $L=8$ transition, but from the relative magnitude of cross sections and the description of the angular pattern an assignment $E_x=5.81$ MeV, $(g_{9/2})^2_{8^+}$ and $E_x=6.03$ MeV, $(g_{9/2},d_{5/2})_{6^+}$ is preferred.

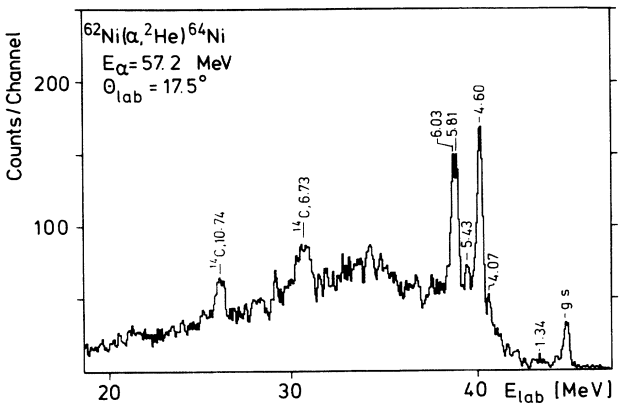

FIG. 14. Spectrum of the ^{62}Ni(α,^{2}He)^{64}Ni reaction at $E_\alpha=57.2$ MeV and $\theta_{lab}=17.5°$.

Based on the DWBA calculations, a significant excitation of the $(f_{5/2},d_{5/2})_{5^-}$ configuration is expected additionally. It might be identified with the level at 5.43 MeV which is compatible with the shape of the angular distribution but leads to a normalization about five times too small, or it might be hidden under the 5.81- and 6.03-MeV states.

7. ^{64}Ni(α,^{2}He)^{66}Ni

Figures 16 and 17 display a spectrum of the reaction and the angular distributions of strong transitions, respectively. Two very tentative $L=5$ assignments can be suggested for the states at 3.39 and 4.76 MeV. The ex-

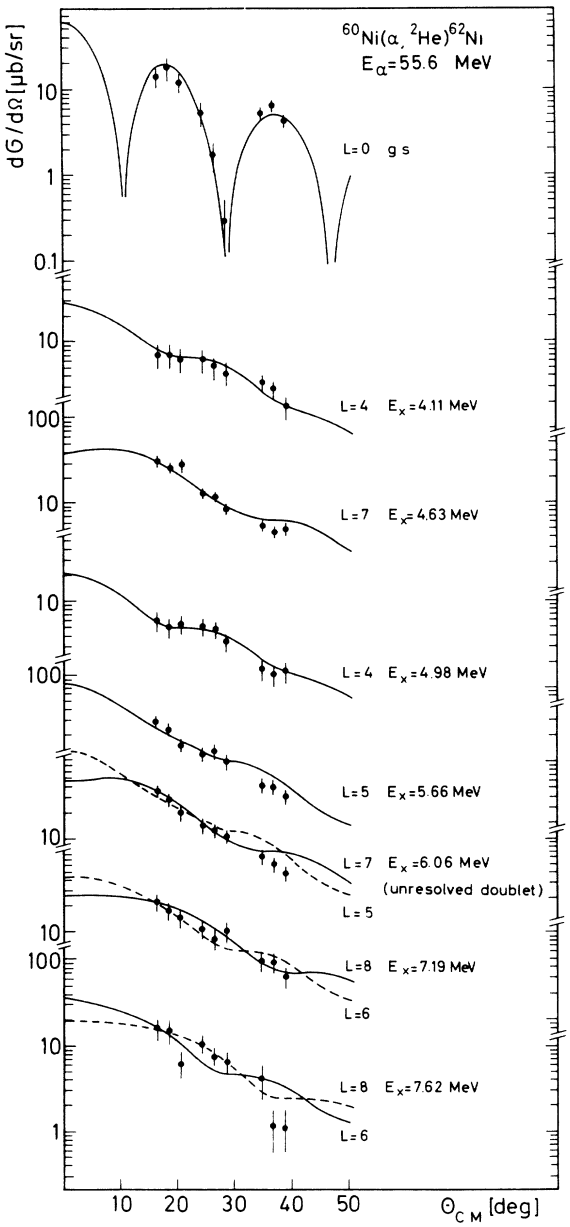

FIG. 13. Angular distributions of transitions to states populated in the ^{60}Ni(α,^{2}He)^{62}Ni reaction. The curves are DWBA calculations. See text.

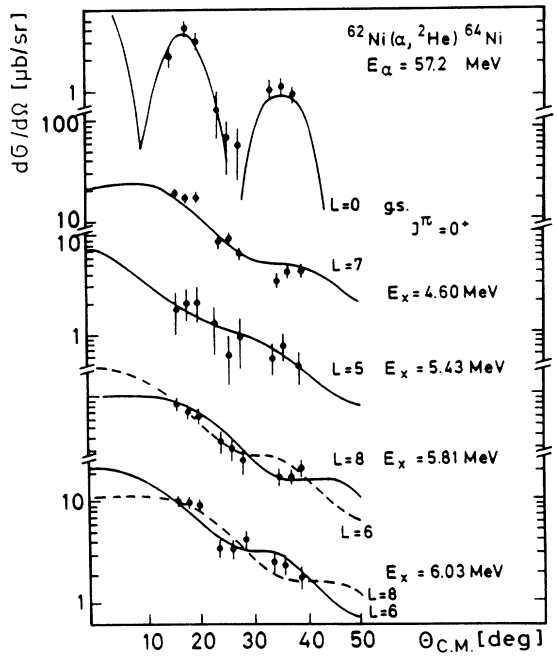

FIG. 15. Angular distributions of transitions to states populated in the ^{62}Ni(α,^{2}He)^{64}Ni reaction. The curves are DWBA calculations. See text.

TABLE IX. DWBA calculations for prominent transitions of the ^{62}Ni$(\alpha,{}^2$He$)^{64}$Ni reaction.

E_x (MeV)	J^π	nn configuration	N
g.s.	0^+	$(p_{1/2})^2_{0^+}$	160±50
4.60	7^-	$(f_{5/2},g_{9/2})_{7^-}$	50±10
5.43	5^-	$(f_{5/2},d_{5/2})_{5^-}$	10±5
5.81	8^+	$(g_{9/2})^2_{8^+}$	60±5
	6^+	$(g_{9/2},d_{5/2})_{6^+}$	30±5
6.03	6^+	$(g_{9/2},d_{5/2})_{6^+}$	50±10
	8^+	$(g_{9/2})^2_{8^+}$	70±5

perimental data points show a relatively large spreading, which prevents a definite conclusion. Nevertheless a $(p_{1/2},g_{9/2})_{5^-}$ calculation yields a normalization well within the range of the other values collected in Table X. At the largest angle measured, the 4.76-MeV level could not be separated clearly from the dominant 5.17-MeV peak. However, the DWBA predicts a reasonable cross section for a $(f_{5/2},d_{5/2})_{5^-}$ configuration normalized at the forward angles.

An $L=7$ transfer is proposed for the 4.06-MeV state due to the very good agreement of the experimental and calculated angular shape. The strongest peak in the spectrum at 5.17 MeV is interpreted as an $L=8+L=6$ doublet. Calculations for a single $L=8$ or $L=6$ transition reproduce the experimental angular distribution reasonable well, but the resulting normalization constants are very large. Almost identical excitation energies are further predicted by the weak-coupling model for the $(g_{9/2})^2_{8^+}$ and $(g_{9/2},d_{5/2})_{6^+}$ configurations in ^{66}Ni (see Sec. V A).

8. ^{64}Zn$(\alpha,{}^2$He$)^{66}$Zn

A spectrum of this reaction, displayed in Fig. 18, exhibits a very similar picture as observed in the ^{62}Ni$(\alpha,{}^2$He$)^{64}$Ni reaction where the target differs only by two protons. Angular distributions for the three prominent peaks and the rather weak transition to a state at 4.68 MeV are given in Fig. 19. Results of the DWBA calculations are presented in Table XI.

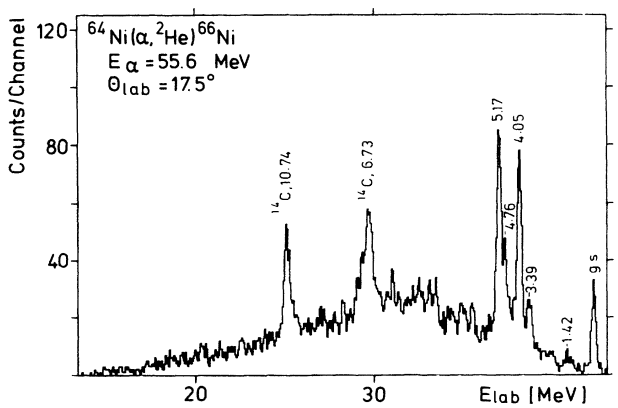

FIG. 16. Spectrum of the ^{64}Ni$(\alpha,{}^2$He$)^{66}$Ni reaction at $E_\alpha=55.6$ MeV and $\theta_{\mathrm{lab}}=17.5°$.

TABLE X. DWBA calculations for prominent transitions of the ^{64}Ni$(\alpha,{}^2$He$)^{66}$Ni reaction.

E_x (MeV)	J^π	nn configuration	N
g.s.	0^+	$(f_{5/2})^2_{0^+}$	8500±700
3.39	5^-	$(p_{1/2},g_{9/2})_{5^-}$	100±40
4.05	7^-	$(f_{5/2},g_{9/2})_{7^-}$	90±20
4.76	5^-	$(f_{5/2},d_{5/2})_{5^-}$	110±40
	8^+	$(g_{9/2})^2_{8^+}$	180±70
5.17	8^+	$(g_{9/2})^2_{8^+}$	
	+	+	130±50[a]
	6^+	$(g_{9/2},d_{5/2})_{6^+}$	
	6^+	$(g_{9/2},d_{5/2})_{6^+}$	230±90
	8^+	$(g_{9/2})^2_{8^+}$	390±150

[a]DWBA calculation for a $(g_{9/2})^2_{8^+}+(g_{9/2},d_{5/2})_{6^+}$ doublet.

The dominant state at 4.22 MeV includes a small contribution from a state at about 4.40 MeV, visible at some of the backward angles. The main transition is expected

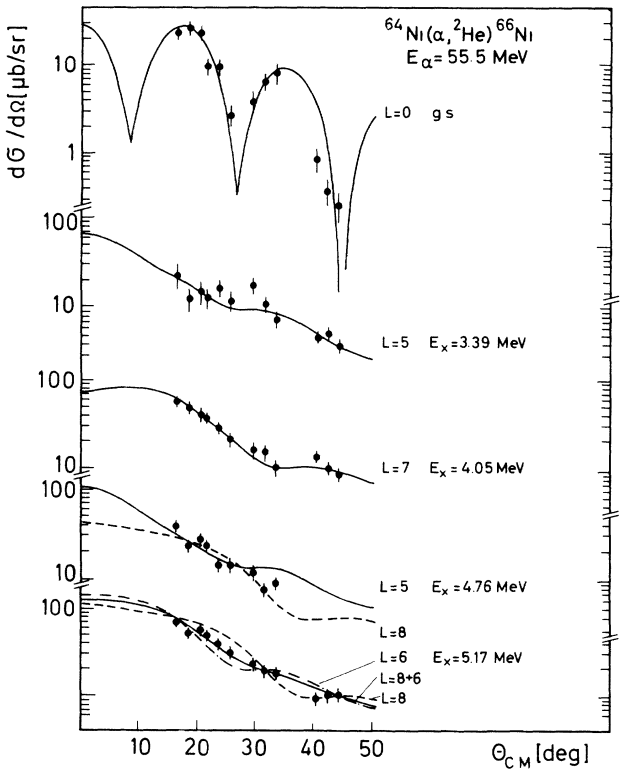

FIG. 17. Angular distributions of transitions to states populated in the ^{64}Ni$(\alpha,{}^2$He$)^{66}$Ni reaction. The curves are DWBA calculations. See text.

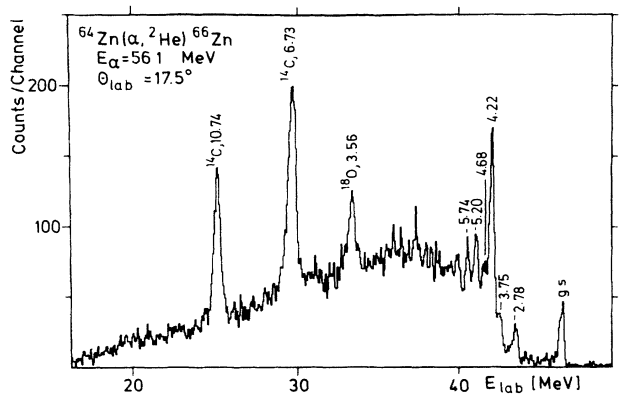

FIG. 18. Spectrum of the ^{64}Zn(α,^{2}He)^{66}Zn reaction at $E_\alpha = 56.1$ MeV and $\theta_{lab} = 17.5°$.

to be $(f_{5/2},g_{9/2})_{7^-}$ while a tentative $(p_{1/2},g_{9/2})_{5^-}$ configuration was assumed for the second state in the DWBA calculation. The angular distribution and absolute cross sections are described satisfactorily by an $L=7$ transfer, while the addition of an $L=5$ state does not affect the results very much. The dominant $(f_{5/2},g_{9/2})_{7^-}$ structure is further confirmed through the identification of a 7^- transition at 4.25 MeV in the ^{64}Ni($\alpha,nn\gamma$)^{66}Ni reaction,[29] which is interpreted by the authors of Ref. 29 as a two-quasiparticle state with a likely $(f_{5/2},g_{9/2})_{7^-}$ configuration. In addition, a state at 4.26 MeV with a tentative $L=7$ assignment has been observed in a study of the reaction ^{64}Zn(t,p)^{66}Zn.[30] No assignment can be given for the 4.68-MeV level due to the scattering of the experimental cross section. It is noted, however, that the assumption of a $(f_{5/2},d_{5/2})_{5^-}$ configuration leads to a

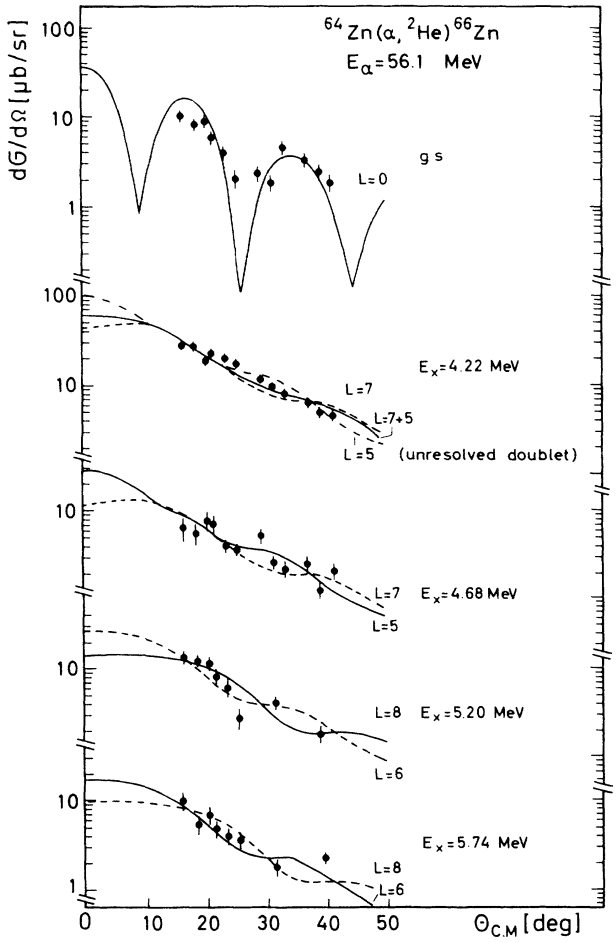

FIG. 19. Angular distributions of transitions to states populated in the ^{64}Zn(α,^{2}He)^{66}Zn reaction. The curves are DWBA calculations. See text.

TABLE XI. DWBA calculations for prominent transitions of the ^{64}Zn(α,^{2}He)^{66}Zn reaction and comparison to other work.

	(α,^{2}He)			Other work[a,b]	
E_x (MeV)	J^π	nn configuration	N	E_x (MeV)	J^π
g.s.	0^+	$(f_{5/2})^2_{0^+}$	11000±4000		
4.22	7^-	$(f_{5/2},g_{9/2})_{7^-}$		4.25[a]	7^-
	+	+	60±10[c]	4.26[b]	(7^-)
	5^-	$(p_{1/2},g_{9/2})_{5^-}$			
	7^-	$(f_{5/2},g_{9/2})_{7^-}$	80±20		
	5^-	$(p_{1/2},g_{9/2})_{5^-}$	220±60		
4.68	5^-	$(f_{5/2},d_{5/2})_{5^-}$	55±20		
	7^-	$(f_{5/2},g_{9/2})_{7^-}$	30±15		
5.20	8^+	$(g_{9/2})^2_{8^+}$	130±40	5.21[a]	8^+
	6^+	$(g_{9/2},d_{5/2})_{6^+}$	65±25		
5.74	6^+	$(g_{9/2},d_{5/2})_{6^+}$	50±15		
	8^+	$(g_{9/2})^2_{8^+}$	95±35		

[a]Reference 29.
[b]Reference 30.
[c]DWBA calculation for a $(f_{5/2},g_{9/2})_{7^-}+(p_{1/2},g_{9/2})_{5^-}$ doublet.

reasonable overall normalization.

At the backward detector positions the partition into three angular areas was abandoned for the 5.20- and 5.74-MeV levels due to the very low statistics compared to the continuous background. Therefore no definite conclusions can be drawn from the comparison of the DWBA with our experimental results. In their investigation of the $^{64}\mathrm{Ni}(\alpha,nn\gamma)^{66}\mathrm{Zn}$ reaction Neal *et al.*[29] observed a $J^\pi=8^+$ transition at 5.21 MeV with a possible $(g_{9/2})^2_{8^+}$ character. This result suggests an $L=8$ assignment for the 5.20-MeV state. For the 5.74-MeV level, a $(g_{9/2},d_{5/2})_{6^+}$ configuration is in agreement with the obtained angular distribution and transition strength.

9. $^{66}Zn(\alpha,{}^2He)^{68}Zn$

A spectrum of this reaction is shown in Fig. 20. Very similar to the $^{64}\mathrm{Ni}(\alpha,{}^2\mathrm{He})^{66}\mathrm{Ni}$ spectrum, two prominent peaks can be seen; their angular distributions are given in Fig. 21. Additionally some transitions of moderate strength at higher-excitation energies could be kinematically identified, but no angular distributions were extracted due to poor statistics. Table XII presents a summary of the DWBA calculations.

The angular distribution of the strong transition at 3.94 MeV contains a contribution from a weaker level at 3.74 MeV which could not be separated at more forward angles. A DWBA calculation assuming $L=7$, $(f_{5/2},g_{9/2})_{7^-}+L=5$, $(p_{1/2},g_{9/2})_{5^-}$ results in a satisfactory description of the experimental angular distribution. The 7^- assignment is supported by a study of the $^{67}\mathrm{Zn}(d,p)^{68}\mathrm{Zn}$ reaction.[31]

The peak at 4.37 MeV is tentatively assigned to be an $L=8+L=6$ doublet. While a pure $L=6$ transition cannot be excluded from the shape and relative strength of the DWBA results, the simultaneous excitation of a $(g_{9/2})^2_{8^+}$ state is very likely: A $J^\pi=8^+$ state at 4.40 MeV has been observed in a study of the $^{65}\mathrm{Cu}(\alpha,p\gamma)^{68}\mathrm{Zn}$ reaction[32] where the authors give a speculative $(g_{9/2})^2_{8^+}$ configuration assignment. Similar to the $^{64}\mathrm{Ni}(\alpha,{}^2\mathrm{He})^{66}\mathrm{Ni}$ reaction, the weak-coupling model predicts nearly identical excitation energies for the 8^+ and 6^+ states.

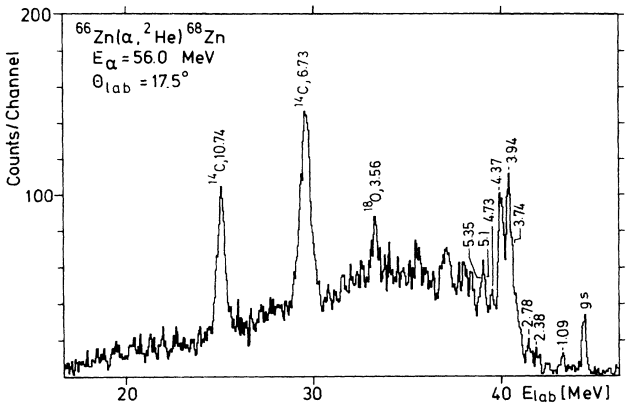

FIG. 20. Spectrum of the $^{66}\mathrm{Zn}(\alpha,{}^2\mathrm{He})^{68}\mathrm{Zn}$ reaction at $E_\alpha=56.0$ MeV and $\theta_{\mathrm{lab}}=17.5°$.

10. $^{70}Ge(\alpha,{}^2He)^{72}Ge$

Figure 22 depicts a spectrum of this reaction at $\theta_{\mathrm{lab}}=17.5°$. No angular distributions are shown due to the following reasons: The spectrum is dominated by a peak, which contains two not fully resolved transitions at 3.74 and 3.99 MeV. Therefore an experimental angular

TABLE XII. DWBA calculations for prominent transitions of the $^{66}\mathrm{Zn}(\alpha,{}^2\mathrm{He})^{68}\mathrm{Zn}$ reaction and comparison to other work.

				Other work[a,b]	
E_x (MeV)	J^π	$(\alpha,{}^2\mathrm{He})$ nn configuration	N	E_x (MeV)	J^π
g.s.	0^+	$(f_{5/2})^2_{0^+}$	3900±3000		
3.90[c]	5^-	$(p_{1/2},g_{9/2})_{5^-}$		3.94[a]	(7^-)
	+	+	40±8[d]		
	7^-	$(f_{5/2},g_{9/2})_{7^-}$			
	7^-	$(f_{5/2},g_{9/2})_{7^-}$	50±10		
	5^-	$(p_{1/2},g_{9/2})_{5^-}$	120±30		
4.37	8^+	$(g_{9/2})^2_{8^+}$		4.40[b]	8^+
	+	+	50±15[e]		
	6^+	$(g_{9/2},d_{5/2})_{6^+}$			
	8^+	$(g_{9/2})^2_{8^+}$	110±25		
	6^+	$(g_{9/2},d_{5/2})_{6^+}$	75±20		

[a]Reference 31.
[b]Reference 32.
[c]Unresolved doublet at 3.74 and 3.94 MeV.
[d]DWBA calculation for a $(f_{5/2},g_{9/2})_{7^-}+(p_{1/2},g_{9/2})_{5^-}$ doublet.
[e]DWBA calculation for a $(g_{9/2})^2_{8^+}+(g_{9/2},d_{5/2})_{6^+}$ doublet.

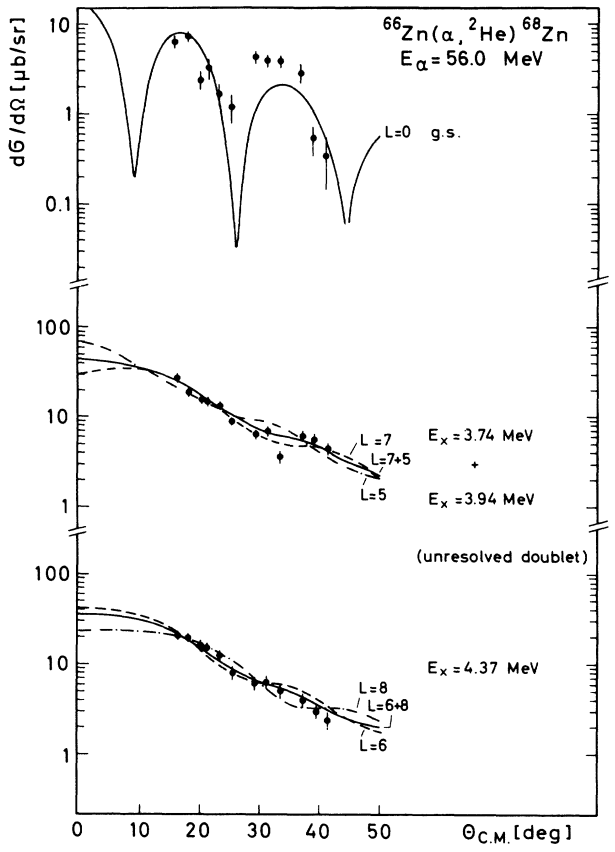

FIG. 21. Angular distributions of transitions to states populated in the ^{66}Zn(α,^{2}He)^{68}Zn reaction. The curves are DWBA calculations. See text.

distribution could only be given for the total peak, and the DWBA information is thus very limited. The yield of the weakly excited states at higher excitation energies is too small relative to the continuous background in order to gain experimental angular distributions at backward angles.

Nevertheless, as a consequence of the filling of the *fp* shell the excitation energies of the expected *nn* high-spin states decrease in the Zn and Ge region and these states can be observed by γ spectroscopy as part of or near the yrast cascade.[29,32–36] From a study of the ^{70}Zn(α,$nn\gamma$)^{72}Ge reaction[33] some conclusions can be drawn. Morand *et al.*[33] identified the states $J^\pi=7^-$, $E_x=3.78$ MeV and $J^\pi=8^+$, $E_x=3.76$ MeV with proposed configurations $(f_{5/2},g_{9/2})_{7^-}$ and $(g_{9/2})^2_{8^+}$, respectively. Since the excitation energy agrees within the quoted error, it is a reasonable assumption to interpret the 3.74-MeV peak as the sum of the $L=7$ and $L=8$ transition. The 3.99-MeV level might then be associated with the $(g_{9/2},d_{5/2})_{6^+}$ configuration.

11. ^{72}Ge(α,^{2}He)^{74}Ge

A spectrum of this reaction is presented in Fig. 23, angular distributions are given in Fig. 24 and DWBA results are collected in Table XIII. The contribution of the 3.87-MeV level to the larger peak at 3.59 MeV could not be unfolded for all angles, so the experimental angular distribution is given for the sum of both.

DWBA calculations for $L=6,7,8$ are compared to the experimental angular distribution of the 4.13-MeV level. No clear distinction can be given from the angular pattern, but $L=7$ or $L=8$ are favored. Therefore, $L=6+L=8$ or $L=6+L=7$, respectively, can be expected for the 3.59-MeV, 3.87-MeV doublet. Regarding the resulting normalization constants a speculative assignment $(g_{9/2},d_{5/2})_{6^+}$ (judged from the relative DWBA strength) for the 3.59-MeV state, $(g_{9/2})^2_{8^+}$ for the 3.87-MeV state, and $(f_{5/2},g_{9/2})_{7^-}$ for the 4.13-MeV state is suggested. However, no clear decision can be made.

The appearance of a strong transition at 6.20 MeV is explained most likely with the transfer of at least one neutron into the $g_{7/2}$ shell. With this assumption possible configurations are $(g_{9/2},g_{7/2})_{8^+}$, $(d_{5/2},g_{7/2})_{6^+}$, and $(g_{7/2})^2_{6^+}$. The binding energy of the $g_{7/2}$ single-particle state is not known experimentally in ^{73}Ge. However, the experimental data available on other nuclei allowed a weak-coupling model calculation (as described in Sec. V A) for $g_{7/2}$ single-particle states. A value $E_B=-3.34$ MeV was extrapolated for ^{73}Ge and used in the DWBA calculation. The shape of the angular distribution of the

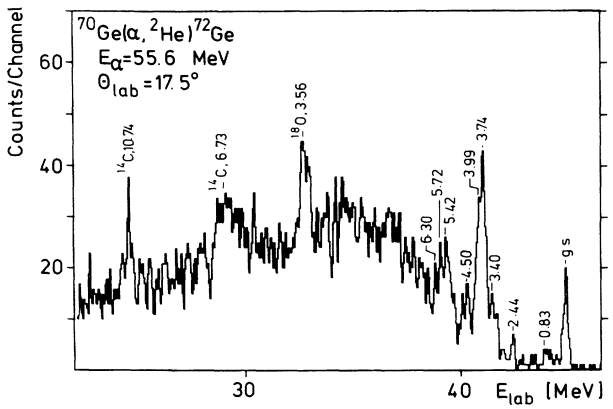

FIG. 22. Spectrum of the ^{70}Ge(α,^{2}He)^{72}Ge reaction at $E_\alpha=55.6$ MeV and $\theta_{lab}=17.5°$.

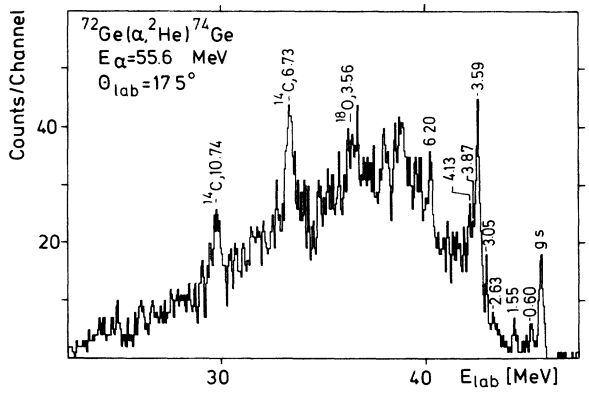

FIG. 23. Spectrum of the ^{72}Ge(α,^{2}He)^{74}Ge reaction at $E_\alpha=55.6$ MeV and $\theta_{lab}=17.5°$.

6.20-MeV state strongly favors $L=6$ in comparison to $L=8$. Due to the very small DWBA cross section for a $(g_{7/2})^2_{6^+}$ configuration, $(d_{5/2},g_{7/2})_{6^+}$ seems most probable, but the normalization constants depend sensitively on the $g_{7/2}$ single-particle energy used.

12. Discussion

The selectivity of the $(\alpha,^2He)$ reaction on fp-shell targets has been well established in the data just presented. Although definite assignments from the comparison of experimental angular distributions with DWBA calculations cannot be attained in all cases, a very consistent description arises from the assumption of a preferential population of $(f_{5/2},g_{9/2})_{7^-}$, $(g_{9/2})^2_{8^+}$, and $(g_{9/2},d_{5/2})_{6^+}$ configurations in all final nuclei. In the Zn and Ge region, where the increase of the continuous background relative to the discrete ^2He lines hinders the establishment of spin assignments, results from γ-decay studies permit an additional comparison.[29,32,33] Agreement is found for all assignments with proposed dominant nn character.

The background continuum observed in all spectra is well understood to originate from sequential statistical two-proton emission. The mass dependence and angular shape can be reproduced with fusion-evaporation calculations.[5]

The cross sections of the $(\alpha,^2He)$ reaction are consistently about 50 times smaller than those of the (α,d) reaction[9] studied under identical experimental conditions. A similar ratio has been observed between nn and pn transfer in light heavy-ion reactions.[6]

Based on all reliably established high-spin assignments, an overall normalization constant $\bar{N}=85\pm45$ is obtained for the $(\alpha,^2He)$ reaction in the fp shell. A direct comparison of this value to the results of Refs. 3 and 5 is not possible, since a different integration interval of the relative pp energy was used.

TABLE XIII. DWBA calculations for prominent transitions of the $^{72}Ge(\alpha,^2He)^{74}Ge$ reaction.

E_x (MeV)	J^π	nn configuration	N
g.s.	0^+	$(g_{9/2})^2_{0^+}$	5700±3500
3.67[a]	6^+	$(g_{9/2},d_{5/2})_{6^+}$	
	+	+	95±25[b]
	8^+	$(g_{9/2})^2_{8^+}$	
	6^+	$(g_{9/2},d_{5/2})_{6^+}$	
	+	+	60±15[c]
	7^-	$(f_{5/2},g_{9/2})_{7^-}$	
4.13	7^-	$(f_{5/2},g_{9/2})_{7^-}$	50±12
	8^+	$(g_{9/2})^2_{8^+}$	180±45
	6^+	$(g_{9/2},d_{5/2})_{6^+}$	65±30
6.20	6^+	$(d_{5/2},g_{7/2})_{6^+}$	40±8
	6^+	$(g_{7/2})^2_{6^+}$	2000±400
	8^+	$(g_{9/2},g_{7/2})_{8^+}$	25±10

[a]Unresolved doublet at 3.59 and 3.87 MeV.
[b]DWBA calculation for a $(g_{9/2},d_{5/2})_{6^+}+(g_{9/2})^2_{8^+}$ doublet.
[c]DWBA calculation for a $(g_{9/2},d_{5/2})_{6^+}+(f_{5/2},g_{9/2})_{7^-}$ doublet.

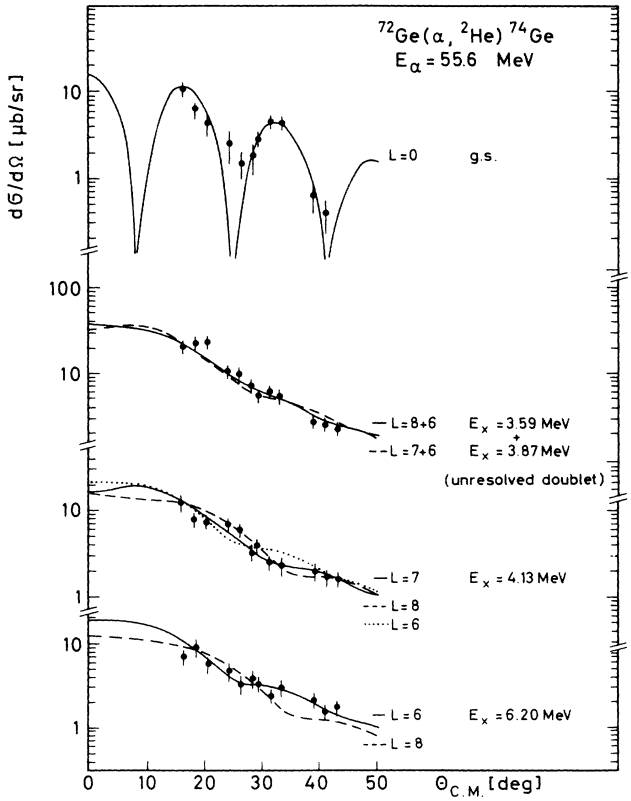

FIG. 24. Angular distributions of transitions to states populated in the $^{72}Ge(\alpha,^2He)^{74}Ge$ reaction. The curves are DWBA calculations. See text.

B. Cr and Ca targets

1. $^{54}Cr(\alpha,^2He)^{56}Cr$

Figures 25 and 26 present a spectrum of this reaction and angular distributions of the prominent transitions,

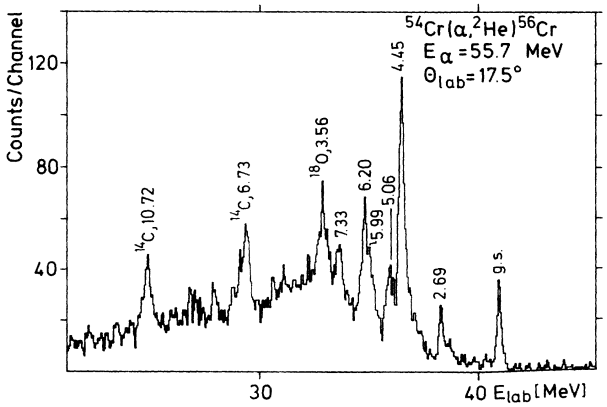

FIG. 25. Spectrum of the $^{54}Cr(\alpha,^2He)^{56}Cr$ reaction at $E_\alpha=55.8$ MeV and $\theta_{lab}=17.5°$.

respectively. Table XIV summarizes the DWBA results. The evaluation of an experimental angular distribution for the dominant transition at 4.45 MeV is impeded by substantial contributions from the contaminant reactions $^{12}C(\alpha,^2He)^{14}C$ (g.s.) and $^{16}O(\alpha,^2He)^{18}O$ (g.s.). The contribution of these reactions at the two forward detector positions was estimated from a measurement of the angular distributions of the $^{12}C(\alpha,^2He)^{14}C$ reaction and a comparison with the results of Ref. 4. However, a large uncertainty remains and the strong oscillations of the g.s. angular distributions render the partition into several angular bins.

A tentative $L=7$ assignment is proposed for the 4.45-MeV state, mainly based on the large experimental cross section which is expected for a $(f_{5/2},g_{9/2})_{7^-}$ configuration from the DWBA computations. The experimental angular distributions shown for the 5.06- and 6.20-MeV peaks again include contributions from smaller states nearby and the DWBA does not permit definite results. Negotiating the data points of the most backward detector position and taking into account the similarity to the $^{56}Fe(\alpha,^2He)^{58}Fe$ spectrum (see Sec. IV A 2), $L=5$ might be expected for both levels. The ratio of the DWBA calculations would then favor a $(f_{5/2},d_{5/2})_{5^-}$ configuration for the 6.20-MeV state and a $(p_{1/2},g_{9/2})_{5^-}$ configuration for the 5.06-MeV state, but both assignments result in large normalization constants compared to the $(f_{5/2},g_{9/2})_{7^-}$ value. A tentative $L=6+L=8$ assignment can be assumed for the 7.33-MeV state, supported by the resulting normalization relative to the 7^- state and the corresponding single-particle excitation energies.

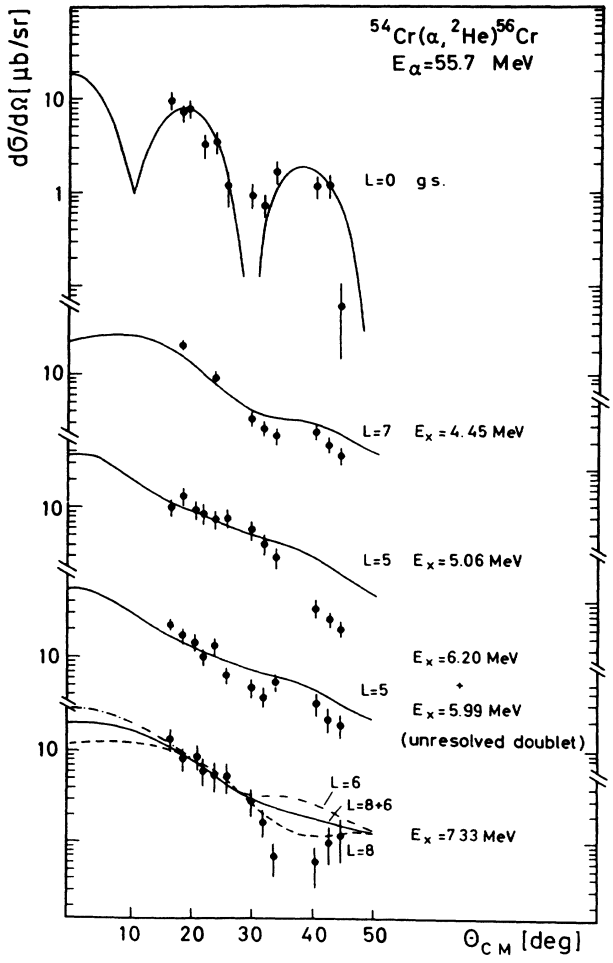

FIG. 26. Angular distributions of transitions to states populated in the $^{54}Cr(\alpha,^2He)^{56}Cr$ reaction. The curves are DWBA calculations. See text.

2. $^{52}Cr(\alpha,^2He)^{54}Cr$

Because of counter problems during data acquisition of the two forward angles, a spectrum of this reaction is shown for $\theta_{lab}=30°$ (Fig. 27). At this angle, the high-spin states no longer dominate the spectrum due to the faster decrease of the angular distributions compared to transitions with lower spin. The energy resolution at the two most forward detector positions was considerably reduced and the states at 8.99 and 9.42 MeV had to be treated as an unresolved doublet in the data analysis. The 6.92-MeV level corresponds to a lower-spin transition and could not be analyzed in the forward angle data. Angular distributions are shown in Fig. 28 and DWBA results are presented in Table XV.

The experimental angular distributions of the states at 3.98 and 4.90 MeV are best described by $L=4$. The data points for the most prominent level at 5.84 MeV show some scattering, so that a clear distinction of the transferred angular momentum is not possible. This state most likely corresponds to a $(f_{5/2},g_{9/2})_{7^-}$ configuration based on the large cross section systematically observed in this study for $L=7$ transitions.

For the second largest peak at 7.20 MeV, $L=5$ with a $(f_{5/2},d_{5/2})_{5^-}$ configuration is proposed which permits a good reproduction of the angular behavior and leads to a normalization well within the range of the other stretched configurations. A calculation for $L=8+L=6$ gives a good description of the summed 8.99, 9.42-MeV

TABLE XIV. DWBA calculations for prominent transitions of the $^{54}Cr(\alpha,^2He)^{56}Cr$ reaction.

E_x (MeV)	J^π	nn configuration	N
g.s.	0^+	$(p_{3/2})^2_{0^+}$	200±70
4.45	7^-	$(f_{5/2},g_{9/2})_{7^-}$	35±10
5.06	5^-	$(p_{1/2},g_{9/2})_{5^-}$	85±30
6.15[a]	5^-	$(f_{5/2},d_{5/2})_{5^-}$	100±40
7.33	8^+	$(g_{9/2})^2_{8^+}$	
	+	+	40±15[b]
	6^+	$(g_{9/2},d_{5/2})_{6^+}$	
	8^+	$(g_{9/2})^2_{8^+}$	100±25
	6^+	$(g_{9/2},d_{5/2})_{6^+}$	50±20

[a]Unresolved doublet at 5.99 and 6.20 MeV.
[b]DWBA calculation for a $(g_{9/2})^2_{8^+}+(g_{9/2},d_{5/2})_{6^+}$ doublet.

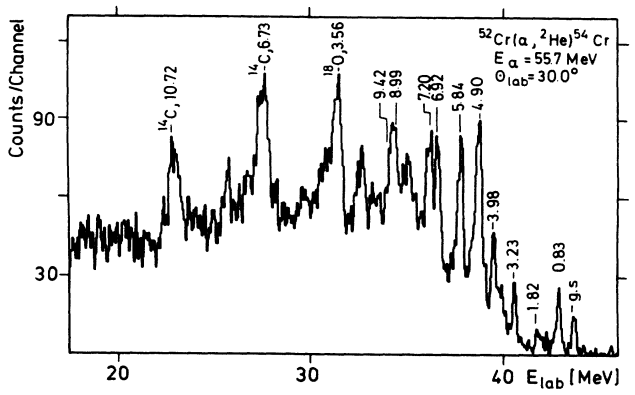

FIG. 27. Spectrum of the $^{52}\mathrm{Cr}(\alpha,{}^2\mathrm{He})^{54}\mathrm{Cr}$ reaction at $E_\alpha=55.8$ MeV and $\theta_{\mathrm{lab}}=30°$.

experimental angular distribution, and the resulting normalization constant agrees with the results for the 5^- and 7^- states. Tentative assignments 8.99 MeV, $(g_{9/2})^2_{8^+}$ and 9.42 MeV, $(g_{9/2},d_{5/2})_{6^+}$ can be suggested, which would reflect the spacing of the $g_{9/2}$ and $d_{5/2}$ single-particle energies in ^{53}Cr (Ref. 37).

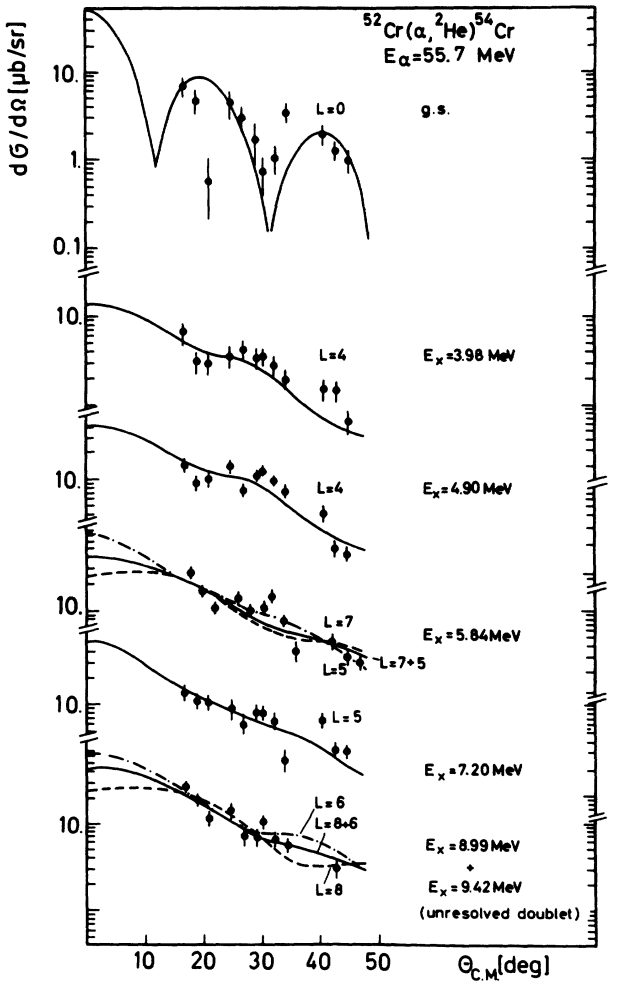

FIG. 28. Angular distributions of transitions to states populated in the $^{52}\mathrm{Cr}(\alpha,{}^2\mathrm{He})^{54}\mathrm{Cr}$ reaction. The curves are DWBA calculations. See text.

TABLE XV. DWBA calculations for prominent transitions of the $^{52}\mathrm{Cr}(\alpha,{}^2\mathrm{He})^{54}\mathrm{Cr}$ reaction.

E_x (MeV)	J^π	nn configuration	N
g.s.	0^+	$(p_{3/2})^2_{0^+}$	230±60
3.98	4^+	$(p_{3/2},f_{5/2})_{4^+}$	60±15
4.90	4^+	$(p_{3/2},f_{5/2})_{4^+}$	170±50
5.84	7^-	$(f_{5/2},g_{9/2})_{7^-}$	45±10
7.20	5^-	$(f_{5/2},d_{5/2})_{5^-}$	50±15
9.28[a]	8^+	$(g_{9/2})^2_{8^+}$	
	+	+	50±15[b]
	6^+	$(g_{9/2},d_{5/2})_{6^+}$	

[a]Unresolved doublet at 8.99 and 9.42 MeV.
[b]DWBA calculation for a $(g_{9/2})^2_{8^+}+(g_{9/2},d_{5/2})_{6^+}$ doublet.

3. $^{50}Cr(\alpha,{}^2He)^{52}Cr$

A spectrum of this reaction is displayed in Fig. 29. For the first target of the present study with a partially open $f_{7/2}$ shell one recognizes a growth in the number of moderately populated final states. This indicates that the $f_{7/2}$ shell must be taken into account in the interpretation of the $^{50}\mathrm{Cr}(\alpha,{}^2\mathrm{He})^{52}\mathrm{Cr}$ reaction. A comparison of experimental angular distributions and DWBA calculations is given in Fig. 30.

Two states are observed in the low excitation energy region. Although excitation energies and angular distributions are compatible with the well established[38,39] assignments 2.77 MeV, 4^+ and 3.11 MeV, 6^+, it is doubtful that the states observed in the $(\alpha,{}^2\mathrm{He})$ reaction correspond to these levels. They are generally interpreted in a pure proton $(f_{7/2})^4$ configuration space (see, e.g., Ref. 39). Absolute strength and angular shape indicate $L=4$–6 for the states between 4 and 6 MeV. From the relative magnitude $L=4$ is preferred for the 4.77-MeV level and $L=5,6$ for the others.

The most prominent peak at 7.75 MeV is tentatively assigned $(f_{5/2},g_{9/2})_{7^-}$, mainly based on the absolute transition strength. The rather small normalization constant might be due to a considerable fragmentation of the $f_{5/2}$ strength in ^{51}Cr (Ref. 37). The angular distributions

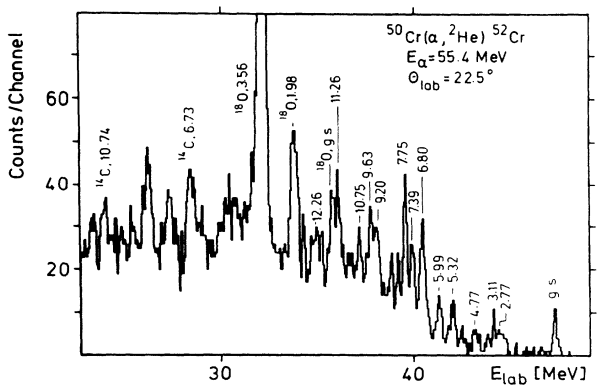

FIG. 29. Spectrum of the $^{50}\mathrm{Cr}(\alpha,{}^2\mathrm{He})^{52}\mathrm{Cr}$ reaction at $E_\alpha=55.4$ MeV and $\theta_{\mathrm{lab}}=22.5°$.

of the states at 6.80 and 7.39 MeV are described similarly well by $L=5$ and $L=7$ transitions. The slightly better reproduction of the 6.80-MeV data by an $L=7$ calculation and the spacing of single-particle levels[37] in ^{51}Cr support the tentative configuration assignments $(f_{7/2},g_{9/2})_{7^-}$, 6.80 MeV and $(p_{1/2},g_{9/2})_{5^-}$, 7.39 MeV, respectively. The 9.20-MeV level is nicely described by a $L=5$ calculation assuming a $(f_{5/2},d_{5/2})_{5^-}$ nn configuration. The angular behavior of the 9.63-MeV peak could not be reproduced by any DWBA calculation.

Three states are unambiguously identified with $E_x > 10$ MeV. Due to the large excitation energies of roughly 4 MeV for the single-particle states in ^{51}Cr, nn configurations based on the coupling of $g_{9/2}$ and $d_{5/2}$ are proposed for these levels. No clear distinction between $L=8$ and $L=6$ can be made from the reproduction of the angular pattern for the states at 10.75, 11.26, and 12.26 MeV. A summary of the DWBA results is found in Table XVI.

4. $^{48}Ca(\alpha,{}^2He)^{50}Ca$

The study of this reaction is of special interest, since a spectrum of rather pure two-particle states can be expected due to the doubly magic target nucleus. So far the only information about ^{50}Ca levels excited through transfer reactions results from investigations of the (t,p) reaction.[40,41] A spectrum of the ^{48}Ca$(\alpha,{}^2$He$)^{50}$Ca reaction is displayed in Fig. 31. The peaks observable at labo-

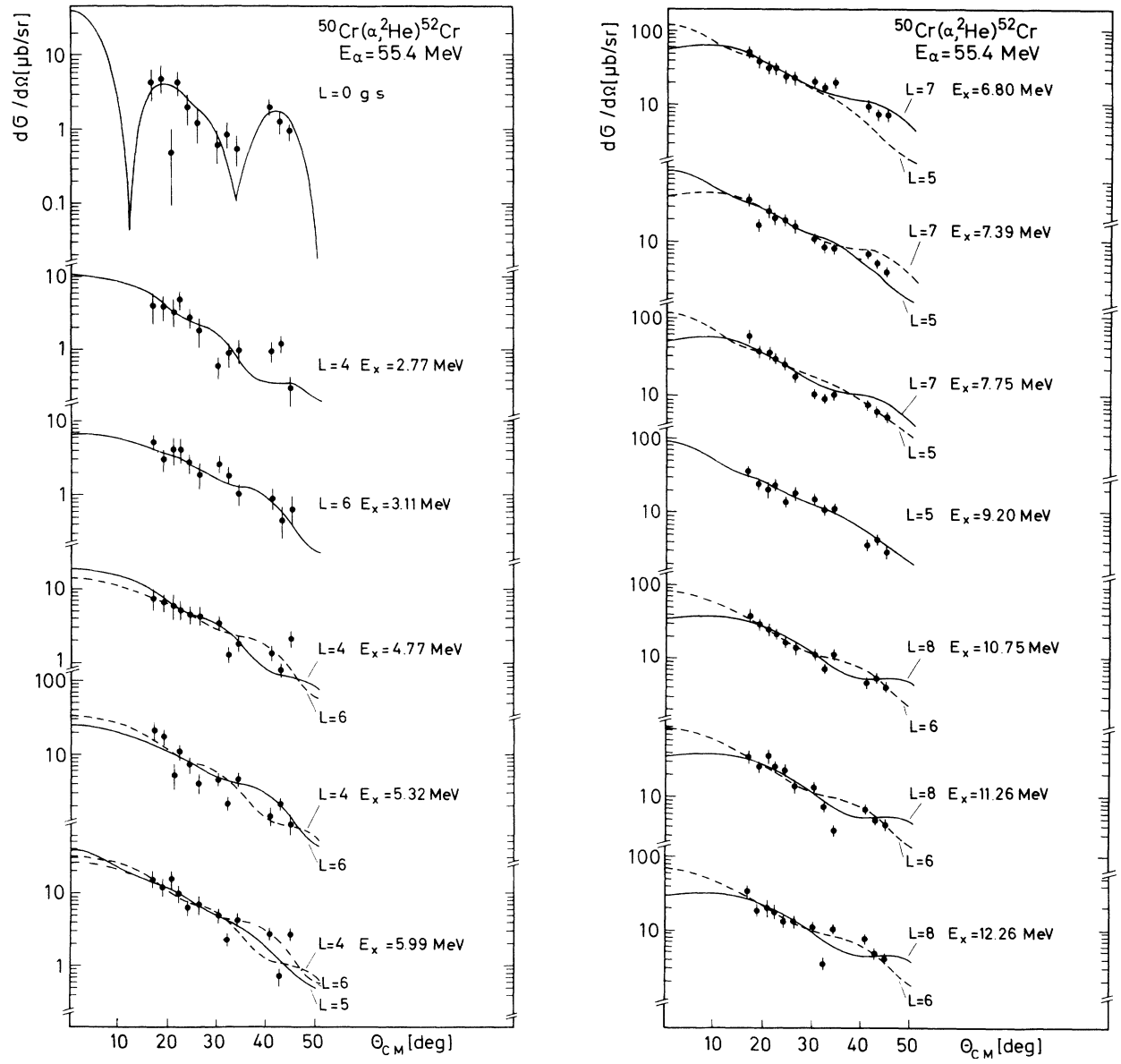

FIG. 30. Angular distributions of transitions to states populated in the ^{50}Cr$(\alpha,{}^2$He$)^{52}$Cr reaction. The curves are DWBA calculations. See text.

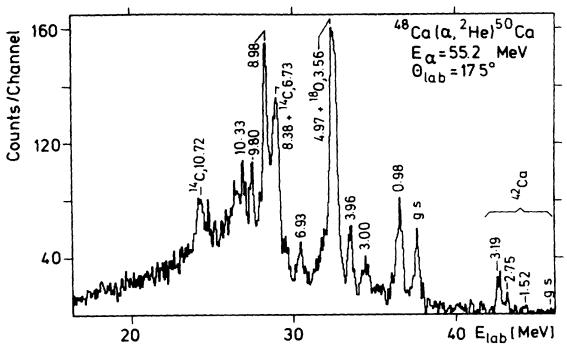

FIG. 31. Spectrum of the ^{48}Ca$(\alpha,{}^2$He$)^{50}$Ca reaction at $E_\alpha=55.3$ MeV and $\theta_{lab}=17.5°$.

ratory energies above 40 MeV arise from a 3% ^{40}Ca impurity in the target. Angular distributions of ^{50}Ca states are given in Fig. 32 and DWBA results in Table XVII. The contamination lines from the $(\alpha,{}^2$He) reaction on ^{12}C and ^{16}O partially inhibit the evaluation of cross sections in some angular distributions.

In contrast to all other g.s. transitions observed in the present study and in contradiction to the DWBA prediction, no oscillations are seen in the experimental g.s. angular distribution of the ^{48}Ca$(\alpha,{}^2$He$)^{50}$Ca reaction. The most probable explanation is the large cross section in the region $E_x=8-9$ MeV for the contaminant reaction ^{40}Ca$(\alpha,{}^2$He$)^{42}$Ca (see Sec. IV B 7), which overlaps with the ^{50}Ca g.s. laboratory energy over the whole angular range measured.

TABLE XVI. DWBA calculations for prominent transitions of the ^{50}Cr$(\alpha,{}^2$He$)^{52}$Cr reaction.

E_x (MeV)	J^π	nn configuration	N
g.s.	0^+	$(f_{7/2})^2_{0^+}$	740±540
2.77	4^+	$(f_{7/2})^2_{4^+}$	200±150
3.11	6^+	$(f_{7/2})^2_{6^+}$	55±15
4.77	4^+	$(p_{3/2},f_{5/2})_{4^+}$	55±33
	6^+	$(f_{7/2},f_{5/2})_{6^+}$	25±13
5.32	6^+	$(f_{7/2},f_{5/2})_{6^+}$	40±15
	4^+	$(p_{3/2},f_{5/2})_{4^+}$	90±60
5.99	6^+	$(f_{7/2},f_{5/2})_{6^+}$	50±20
	5^-	$(f_{7/2},d_{5/2})_{5^-}$	50±30
	4^+	$(p_{3/2},f_{5/2})_{4^+}$	100±50
6.80	7^-	$(f_{7/2},g_{9/2})_{7^-}$	170±40
	5^-	$(f_{5/2},d_{5/2})_{5^-}$	190±50
7.39	5^-	$(p_{1/2},g_{9/2})_{5^-}$	120±30
	7^-	$(f_{7/2},g_{9/2})_{7^-}$	130±30
7.75	7^-	$(f_{5/2},g_{9/2})_{7^-}$	55±20
	5^-	$(f_{5/2},d_{5/2})_{5^-}$	85±25
9.20	5^-	$(f_{5/2},d_{5/2})_{5^-}$	90±15
10.75	8^+	$(g_{9/2})^2_{8^+}$	180±40
	6^+	$(g_{9/2},d_{5/2})_{6^+}$	90±15
11.26	6^+	$(g_{9/2},d_{5/2})_{6^+}$	100±30
	8^+	$(g_{9/2})^2_{8^+}$	190±50
12.26	6^+	$(g_{9/2},d_{5/2})_{6^+}$	110±30
	8^+	$(g_{9/2})^2_{8^+}$	210±70

The angular distribution of the first excited state favors a $J^\pi=2^+$ assignment in agreement with other experiments. The states at 3.00 and 3.96 MeV are likely to correspond to the 3.00- and 3.99-MeV states observed in the (t,p) reaction. However, from the DWBA calculation $L=4$ is favored in both cases at variance with the proposed 3.00-MeV, $L=2$ and 3.99-MeV, $L=3$ assignments.[42] If one assumes a $(p_{3/2},f_{5/2})_{4^+}$ configuration in both cases, taking into account the splitting of the $f_{5/2}$ single-particle state in ^{49}Ca into two states[43] with a strength ratio of $\approx$1:4 and an energy spacing of $\approx$0.5 MeV, a reasonable normalization constant compared to the high-spin states is achieved.

The 4.97-MeV peak consists of a doublet. The best description of the angular distribution is attained by a summed $L=4+L=5$ calculation. The configurations involved remain unclear, but $(p_{1/2},g_{9/2})_{5^-}$ is probable regarding the experimental cross sections.

Four strongly populated states are found above 8 MeV excitation energy. The experimental angular distributions indicate $L\geq 6$ in all cases. The extended measurement at five detector positions allows a rather clear distinction of transferred angular momentum except for the 10.33-MeV level. A $(f_{5/2},g_{9/2})_{7^-}$ configuration is preferred for the states at 8.38 and 8.98 MeV. The appearance of two $L=7$ transitions might be explained again by the splitting of the $f_{5/2}$ strength. The state at 9.80 MeV reveals a clear $L=6$ structure. Therefore $L=8$ rather than $L=6$ is more likely for the 10.33-MeV state, although due to the missing experimental data for $\theta_{c.m.}=35°-50°$ no definite conclusions can be drawn from the DWBA calculations. Adding the strength for the split $(f_{5/2},g_{9/2})_{7^-}$ configuration, all resulting normalization constants are in fair agreement with each other.

5. ^{44}Ca$(\alpha,{}^2$He$)^{46}$Ca

The influence of the open $f_{7/2}$ shell is clearly visible in a spectrum of this reaction (Fig. 33). The number of final states with comparable transition strengths increases strongly. While levels with excitation energies up to 13 MeV could be kinematically identified, the region $E_x=9-12$ MeV was strongly contaminated by the ^{16}O$(\alpha,{}^2$He$)^{18}$O reaction and no data analysis was performed for this region. Figure 34 shows the angular distributions and Table XVIII summarizes the DWBA results.

All low-lying states up to 3-MeV excitation energy correspond to transitions identified in (t,p) (Ref. 40) and (p,t) (Ref. 44) reactions leading to ^{46}Ca. The simultaneous observation of the 2.97-MeV state in the nn pickup reaction (p,t) suggests a pure $(f_{7/2})^2_{6^+}$ character, since a coupling of this configuration to a dominant $(f_{7/2})^4_{0^+}$ g.s. configuration in ^{44}Ca is equivalent to the $(f_{7/2})^{-2}_{6^+}$ configuration proposed in the (p,t) reaction.

No detailed discussion is given for all remaining states. Although in some individual cases a definite L value is

TABLE XVII. DWBA calculations for prominent transitions of the $^{48}Ca(\alpha,^2He)^{50}Ca$ reaction and comparison to other work.

E_x (MeV)	J^π	$(\alpha,^2He)$ *nn* configuration	N	Other work[a] E_x (MeV)	J^π
g.s.	0^+	$(p_{3/2})^2_{0^+}$	380±230		
0.98	2^+	$(p_{3/2})^2_{2^+}$	140±40	1.02	2^+
3.00	4^+	$(p_{3/2},f_{5/2})_{4^+}$		3.00	(2^+)
+			90±35[b]		
3.96	4^+	$(p_{3/2},f_{5/2})_{4^+}$		3.96	(3^-)
4.97	4^+	$(p_{3/2},f_{5/2})_{4^+}$		4.83	(4^+)
	+	+	90±35[c]		
	5^-	$(p_{1/2},g_{9/2})_{5^-}$			
8.38	7^-	$(f_{5/2},g_{9/2})_{7^-}$			
+			60±25[b]		
8.98	7^-	$(f_{5/2},g_{9/2})_{7^-}$			
9.80	6^+	$(g_{9/2},d_{5/2})_{6^+}$	45±10		
	8^+	$(g_{9/2})^2_{8^+}$	60±35		
10.33	8^+	$(g_{9/2})^2_{8^+}$	60±20		
	6^+	$(g_{9/2},d_{5/2})_{6^+}$	40±15		

[a]Reference 42.
[b]Sum of both levels.
[c]DWBA calculation for a $(p_{3/2},f_{5/2})_{4^+}+(p_{1/2},g_{9/2})_{5^-}$ doublet.

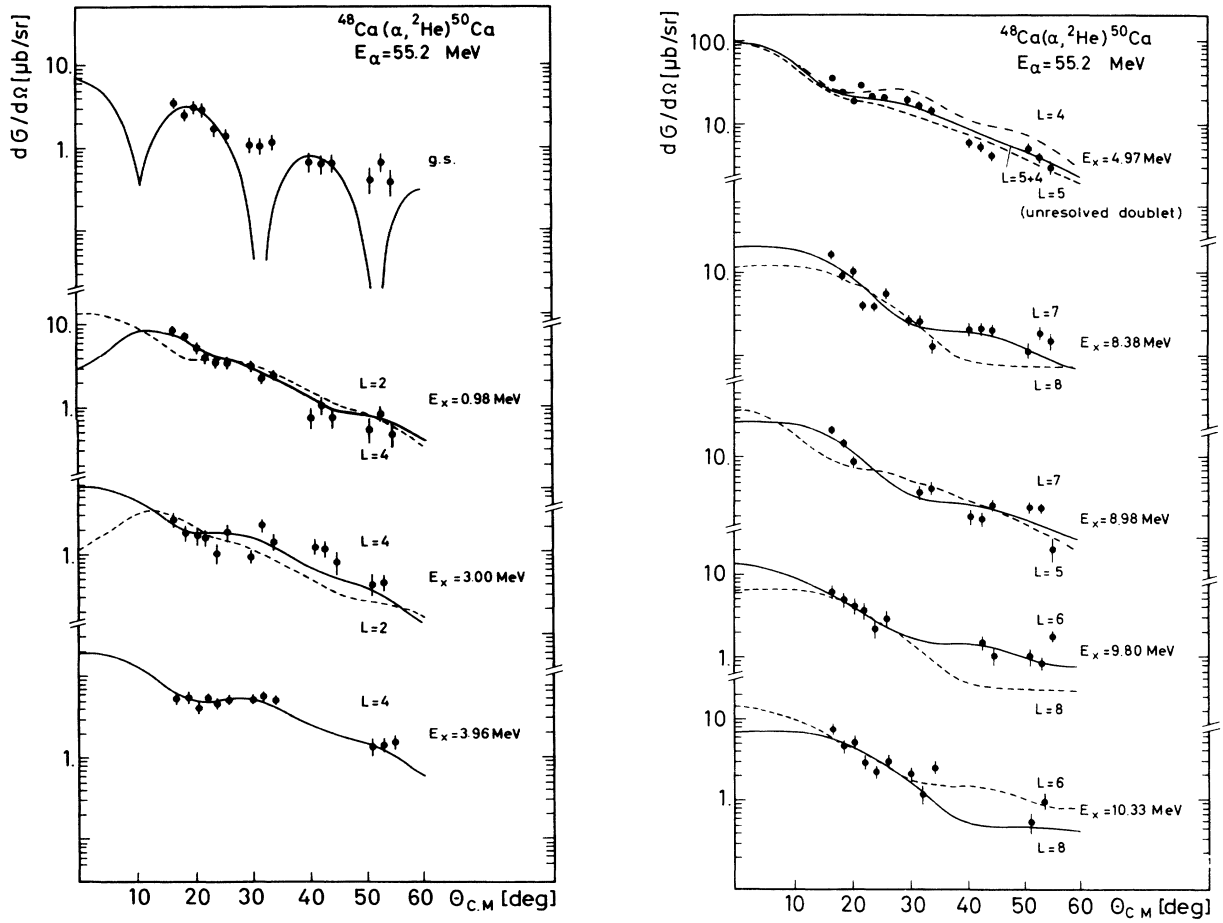

FIG. 32. Angular distributions of transitions to states populated in the $^{48}Ca(\alpha,^2He)^{50}Ca$ reaction. The curves are DWBA calculations. See text.

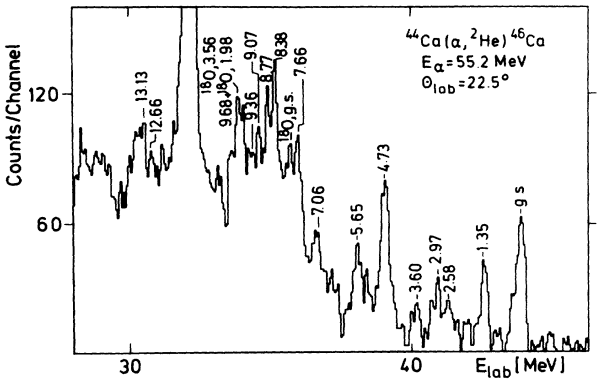

FIG. 33. Spectrum of the ^{44}Ca$(\alpha,{}^2$He$)^{46}$Ca reaction at E_α=55.3 MeV and θ_{lab}=22.5°.

favored from the angular distribution, the information from the angular shape alone is in general inadequate to clearly assign spins. A strong fragmentation of the single-particle states $f_{5/2}$, $g_{9/2}$, $d_{5/2}$, which couple to the high-spin states, is found[39] in ^{45}Ca, and it cannot be excluded that a considerable part of the strength lies above the particle emission threshold. Consequently all normalization constants are small compared to the typical values N=60–150 observed in this study and the concept of stripping into rather pure single-particle levels is no longer useful for the interpretation of the observed spectra. From the steepness of the decrease of the angular distributions we conclude that all states above 3 MeV are likely to have angular momenta $L \geq 5$. The large excitation energies ($E_x > 4.5$ MeV) of the experimentally observed $g_{9/2}$ and $d_{5/2}$ levels indicate that the states above E_x=12 MeV in Fig. 33 are based on $(g_{9/2})^2_{8^+}$ and $(g_{9/2},d_{5/2})_{6^+}$ configurations.

6. ^{42}Ca$(\alpha,{}^2$He$)^{44}$Ca

Figure 35 shows an energy spectrum of the ^{42}Ca$(\alpha,{}^2$He$)^{44}$Ca reaction at θ_{lab}=17.5°. The target includes a 11% ^{40}Ca component leading to a strong contamination line (^{42}Ca, 3.29 MeV, 6^+) indicated in the figure. The number of final states is large above 5 MeV excitation energy and the angular distributions depicted in Fig. 36 are limited to those levels clearly separable at all detection angles.

The g.s. angular distribution is described well by the DWBA. The level is 3.29 MeV is assigned L=6, $(f_{7/2})^2_{6^+}$ from the good correspondence of experimental and calculated angular shape, the normalization constant

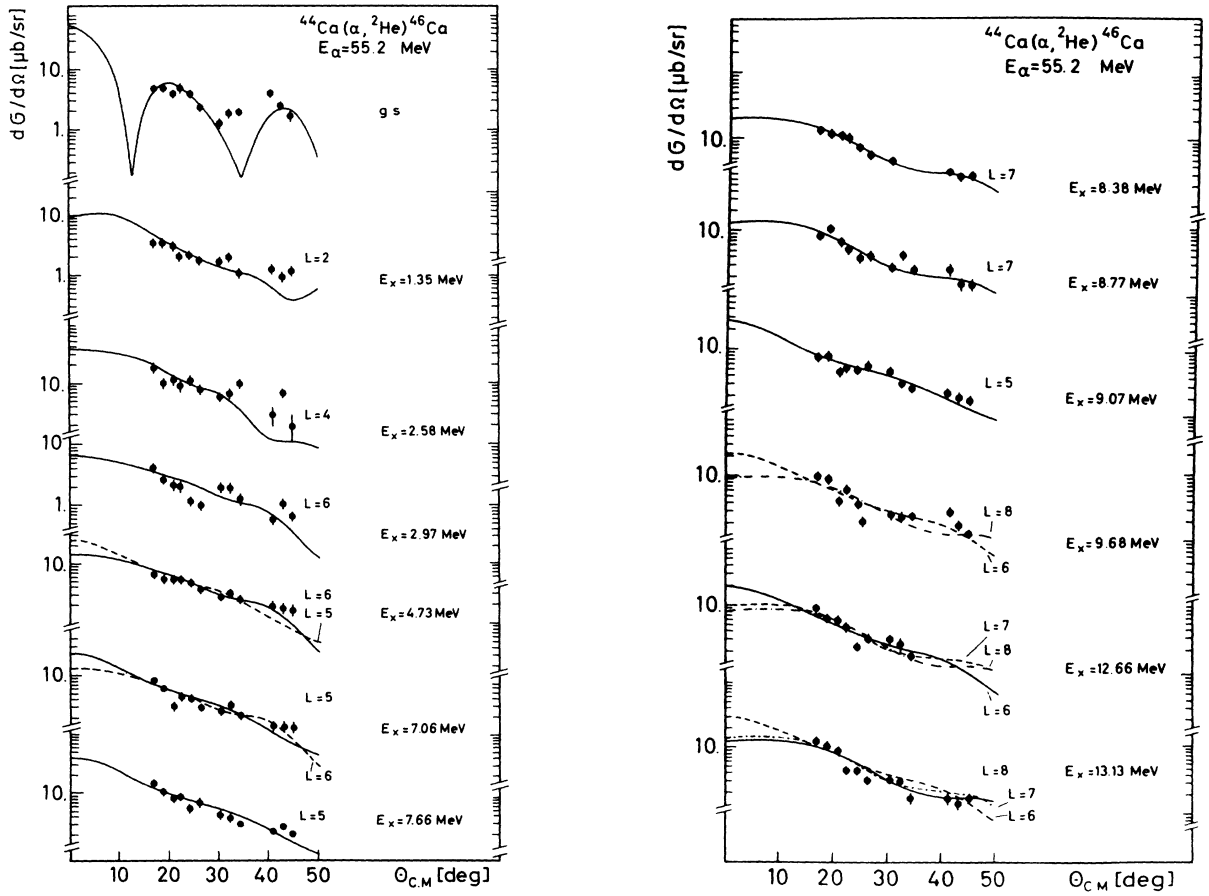

FIG. 34. Angular distributions of transitions to states populated in the ^{44}Ca$(\alpha,{}^2$He$)^{46}$Ca reaction. The curves are DWBA calculations. See text.

TABLE XVIII. DWBA calculations for prominent transitions of the ^{44}Ca(α,^{2}He)^{46}Ca reaction and comparison to other work.

E_x (MeV)	J^π	(α,^{2}He) *nn* configuration	N	Other work[a,b] E_x (MeV)	J^π
g.s.	0^+	$(f_{7/2})^2_{0^+}$	1200±900		
1.35	2^+	$(f_{7/2})^2_{2^+}$	440±140	1.35[a,b]	2^+
2.58	4^+	$(f_{7/2})^2_{4^+}$	45±15	2.57[a,b]	4^+
2.97	6^+	$(f_{7/2})^2_{6^+}$	35±15	2.98[a,b]	6^+
4.73	6^+	$(f_{7/2},f_{5/2})_{6^+}$	23±6		
	5^-	$(f_{7/2},d_{5/2})_{5^-}$	25±10		
7.06	5^-	$(f_{7/2},d_{5/2})_{5^-}$	24±8		
	6^+	$(f_{7/2},f_{5/2})_{6^+}$	30±7		
7.66	5^-	$(f_{5/2},d_{5/2})_{5^-}$	37±12		
8.38	7^-	$(f_{7/2},g_{9/2})_{7^-}$	38±4		
8.77	7^-	$(f_{5/2},g_{9/2})_{7^-}$	12±2		
9.07	5^-	$(p_{1/2},g_{9/2})_{5^-}$	40±8		
9.68	5^-	$(p_{1/2},g_{9/2})_{5^-}$	31±10		
	6^+	$(g_{9/2},d_{5/2})_{6^+}$	13±4		
	8^+	$(g_{9/2})^2_{8^+}$	19±7		
12.66	6^+	$(g_{9/2},d_{5/2})_{6^+}$	25±6		
	8^+	$(g_{9/2})^2_{8^+}$	23±7		
	7^-	$(f_{5/2},g_{9/2})_{7^-}$	26±8		
13.13	6^+	$(g_{9/2},d_{5/2})_{6^+}$	40±9		
	8^+	$(g_{9/2})^2_{8^+}$	53±10		
	7^-	$(f_{5/2},g_{9/2})_{7^-}$	34±8		

[a]Reference 40.
[b]Reference 41.

and the supporting observation of a pure $L=3$ transfer in the ^{43}Ca(d,p)^{44}Ca reaction.[45] The angular distributions of the 4.55- and 5.21-MeV states favor $L=6,7$ and $L=4,5$, respectively, with the 5.21-MeV peak showing a doublet structure.

Since the arguments given in the previous section are valid for the ^{42}Ca(α,^{2}He)^{44}Ca reaction likewise, and a similar fragmentation of the single-particle strength is experimentally observed,[39] a detailed discussion of the angular distributions of all states above $E_x=5.5$ MeV is relinquished. The DWBA results given in Table XIX are only meant as an indication of typical values. It is an interesting aside that several states with moderate strength suggest $L\leq 3$ (e.g., 5.86, 6.21, 9.46 MeV) regarding their angular distributions. Even an $L=0$ transition at 5.86 MeV might have been detected, but this assumption is mainly based on the observation of a 0^+ state at a comparable excitation energy in the ^{42}Ca(t,p)^{44}Ca reaction.[40]

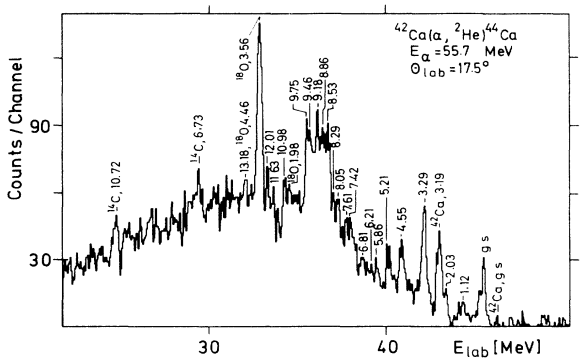

FIG. 35. Spectrum of the ^{42}Ca(α,^{2}He)^{44}Ca reaction at $E_\alpha=55.7$ MeV and $\theta_{lab}=17.5°$.

7. ^{40}Ca(α,^{2}He)^{42}Ca

This reaction has been studied in earlier measurements at 55 MeV (Ref. 4) and 65 MeV (Ref. 5) incident energy. A spectrum of the present investigation is displayed in Fig. 37 at $\theta_{lab}=17.5°$. For all three experiments, the obtained excitation energies agree within the quoted errors. Due to the better energy resolution and the much better statistics compared to Refs. 4 and 5, a number of previously unresolved levels are revealed, especially between 9 and 10 MeV excitation energy.

The states up to 3.19 MeV are very satisfactorily described as members of the $(f_{7/2})^2_{0^+,2^+,4^+,6^+}$ multiplet.[46] No discussion in terms of specific *nn* configurations is performed for the higher-lying states, although their structure should be especially easy to interpret due to the shell closure ($N_n=20$). A recent high-precision measurement of the ^{40}Ca(d,p)^{41}Ca reaction[47] with an energy reso-

lution of ≈ 6 keV and states resolved up to the neutron emission threshold demonstrates that only a small fraction of the $g_{9/2}(20\%)$ and $d_{5/2}(10\%)$ strength is found in the particle bound region. Additionally, a strong fragmentation of the $f_{5/2}$ state is observed with the most prominent level carrying no more than $\approx 15\%$ of the total spectroscopic strength. On the other hand, tentative spin assignments seem to be justified judging the reproduction of the experimental angular distributions shown in Fig. 38 for all levels up to $E_x = 7.28$ MeV.

The decomposition of final states in the broad peak around $E_x \approx 9-10$ MeV is displayed in Fig. 39. Because of a level spacing close to the energy resolution of the detector, large uncertainties of 50–100 % result from the fit procedure using Gaussians. The shape and magnitude of the angular distributions indicate $L \geq 5$ for the major part of the strength. As an example some DWBA calculations are shown for the 9.33-MeV state. Keeping in mind the small spectroscopic factors of the $f_{5/2}$, $g_{9/2}$, $d_{5/2}$ states obtained in Refs. 47 and 48, the normalization constants given in Table XX are reasonable compared to the clearly assigned 3.19 MeV state. However, the large number of possible n and nn states inhibits tentative assignments based on the single-particle structure.

8. *Discussion*

The observed spectra become more complex with decreasing neutron number, and the difficulties to identify high-spin states populated via transfer into the $g_{9/2}$ shell increase strongly. This can be traced back to several reasons: The number of possible states with $L \geq 5$ grows, when transfer into the $f_{7/2}$ shell is allowed. Because of the limitation of the maximum available beam energy (56 MeV) the optimum L window is shifted to $\approx (5-6)\hbar$ for the Ca isotopes. The main problem arises from the strong fragmentation of the relevant single-particle states, which is reflected in a reduced population of the high-

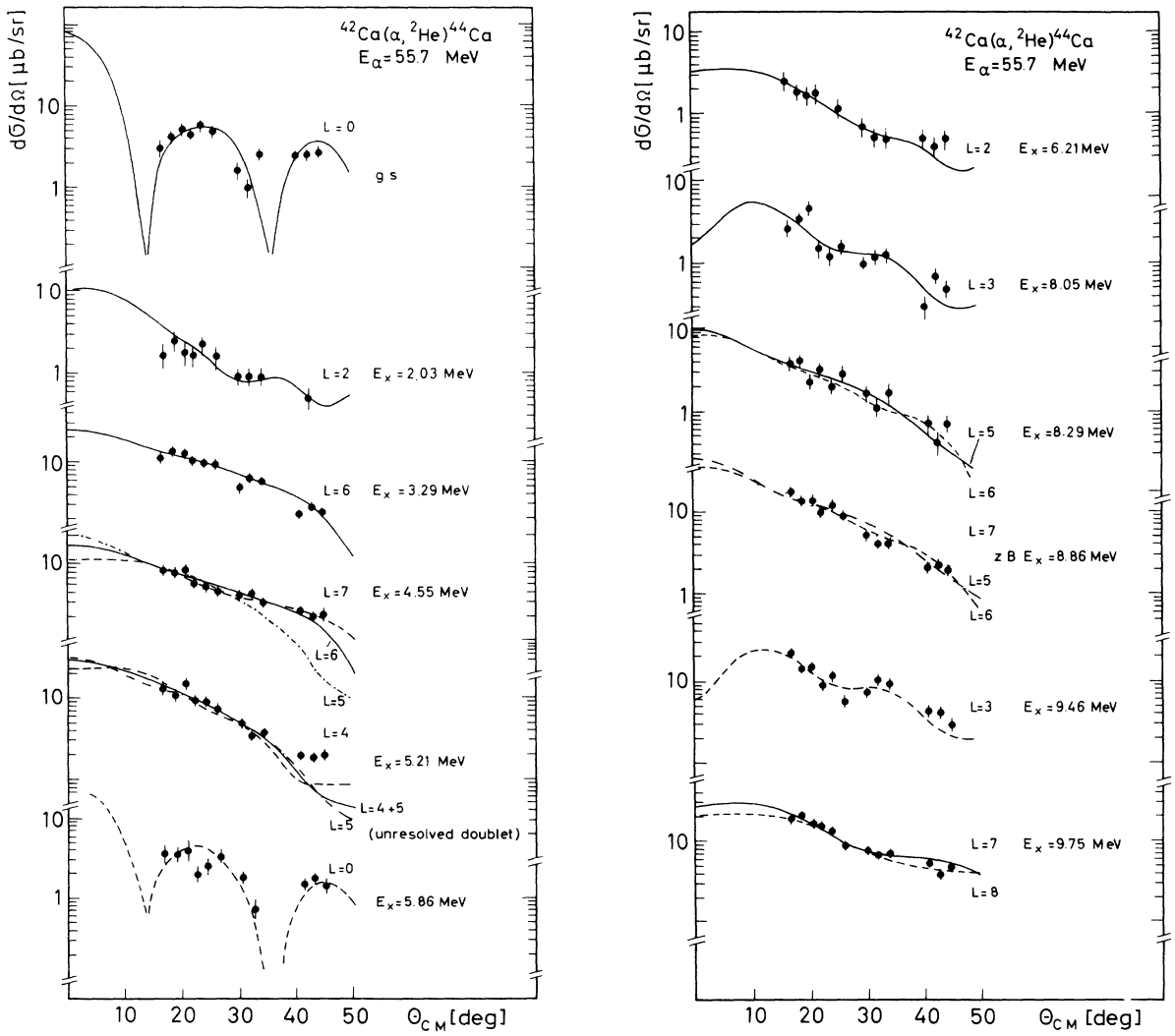

FIG. 36. Angular distributions of transitions to states populated in the ^{42}Ca(α,^{2}He)^{44}Ca reaction. The curves are DWBA calculations. See text.

TABLE XIX. DWBA calculations for prominent transitions of the ^{42}Ca(α,^{2}He)^{44}Ca reaction and comparison to other work.

E_x (MeV)	J^π	(α,^{2}He) *nn* configuration	N	Other work[a,b] E_x (MeV)	J^π
g.s.	0^+	$(f_{7/2})^2_{0^+}$	1000±280		
2.03	2^+	$(f_{7/2})^2_{0^+}$	33±10		
3.29	6^+	$(f_{7/2})^2_{6^+}$	80±20	3.30[a,b]	(6^+)
4.55	6^+	$(f_{7/2},f_{5/2})_{6^+}$	15±5		
	7^-	$(f_{7/2},g_{9/2})_{7^-}$	11±2		
5.21[c]	4^+	$(f_{7/2},p_{1/2})_{4^+}$			
	+	+	21±6[d]		
	5^-	$(f_{7/2},d_{5/2})_{5^-}$			
5.86	0^+	$(p_{1/2})^2_{0^+}$	1700±500	5.86[a]	(0^+)
6.21	2^+	$(p_{3/2})^2_{2^+}$	40±15		
8.05	3^-	$(p_{1/2},d_{5/2})_{3^-}$	10±4		
8.29	5^-	$(p_{1/2},g_{9/2})_{5^-}$	10±4		
8.86	5^-	$(f_{5/2},d_{5/2})_{5^-}$	23±7		
	6^+	$(g_{9/2},d_{5/2})_{6^+}$	13±4		
	7^-	$(f_{5/2},g_{9/2})_{7^-}$	32±11		
9.46	3^-	$(p_{1/2},d_{5/2})_{3^-}$	70±15		
9.75	7^-	$(f_{5/2},g_{9/2})_{7^-}$	22±5		
	8^+	$(g_{9/2})^2_{8^+}$	40±8		

[a]Reference 40.
[b]Reference 45.
[c]Unresolved doublet.
[d]DWBA calculation for a $(f_{7/2},p_{1/2})_{4^+}+(f_{7/2},d_{5/2})_{5^-}$ doublet.

spin states, respectively, small normalization constants.

It should be noted that the selectivity of the (α,^{2}He) to populate fully stretched *nn* configurations is not affected by the experimental problems discussed above. It is well known that the g.s. configurations of ^{41,43,45}Ca carry the main part of the $f_{7/2}$ spectroscopic strength. Accordingly the $(f_{7/2})^2_{6^+}$ configuration is strongly populated in ^{42,44,46}Ca and the resulting normalization constants compare well with those of the high-spin states discussed in Sec. IV A.

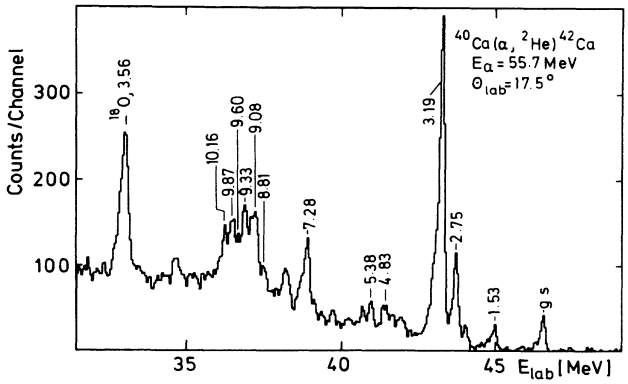

FIG. 37. Spectrum of the ^{40}Ca(α,^{2}He)^{42}Ca reaction at E_α=55.3 MeV and θ_{lab}=17.5°.

V. SYSTEMATICS

The large amount of data obtained in the present investigation made it possible to study the systematics of $(f_{5/2},g_{9/2})_{7^-}$, $(g_{9/2})^2_{8^+}$ and $(g_{9/2},d_{5/2})_{6^+}$ states. Table XXI lists the excitation energies of the high-spin states extracted from the experimental results. These data have been partly presented already in Ref. 49. For a few final nuclei, the excitation energies differ up to 150 keV, because data were reanalyzed for consistency and the measurements were extended in the meantime. Also included are the few data about stretched *nn* states from experimental work on final nuclei which are not accessible by the (α,^{2}He) reaction.

The binding energies of these states are compared to two simple shell-model approaches, the weak-coupling model of Bansal and French[50,51] and a crude shell model.[10] Finally, the experimentally observed 7^- and 8^+ states are compared to a large configuration space shell-model calculation, which was performed not using the results of the present experiment as input parameters. Thus, the resulting excitation energies and wave functions of the 7^- and 8^+ states provide a sensitive test of the assumption of pure configurations.

A. Weak-coupling model

In a study of the (α,^{2}He) reaction on *sd* shell targets a linear dependence of the binding energies B_{2n} of the

TABLE XX. DWBA calculations for prominent transitions of the $^{40}\mathrm{Ca}(\alpha,{}^2\mathrm{He})^{42}\mathrm{Ca}$ reaction and comparison to other work.

E_x (MeV)	J^π	$(\alpha,{}^2\mathrm{He})$ nn configuration	N	Other work[a,b,c] E_x (MeV)	J^π
g.s.	0^+	$(f_{7/2})^2_{0^+}$	260±20		
1.53	2^+	$(f_{7/2})^2_{2^+}$	260±20	1.52[a]	2^+
2.75	4^+	$(f_{7/2})^2_{4^+}$	180±15	2.75[a,b,c]	4^+
3.19	6^+	$(f_{7/2})^2_{6^+}$	120±5	3.19[a,b,c]	6^+
4.83	4^+	$(f_{7/2},p_{3/2})_{4^+}$	30±4		
5.38	6^+	$(f_{7/2},f_{5/2})_{6^+}$	9±1		
7.28	6^+	$(f_{7/2},f_{5/2})_{6^+}$	6±1	7.40[b],7.51[c]	

[a]Reference 23.
[b]Reference 4.
[c]Reference 5.

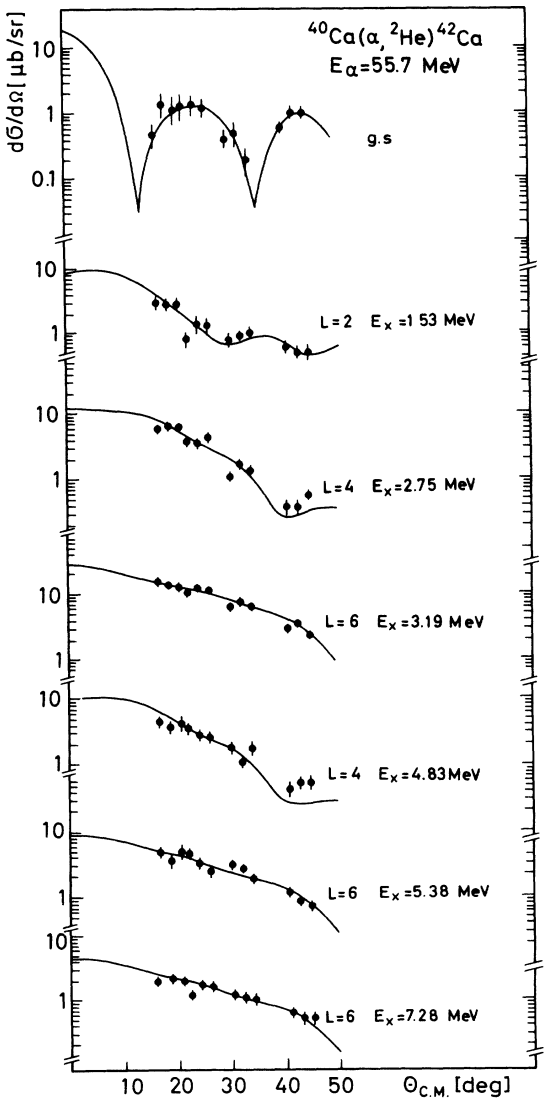

FIG. 38. Angular distributions of transitions to states populated in the $^{40}\mathrm{Ca}(\alpha,{}^2\mathrm{He})^{42}\mathrm{Ca}$ reaction. The curves are DWBA calculations. See text.

$(f_{7/2})^2_{6^+}$ and $(d_{3/2},f_{7/2})_{5^-}$ configurations on the mass number of the final nuclei was observed.[4] This behavior could be successfully described by the weak-coupling model (WCM). A similar linear dependence on the mass number A and the isospin T can be expected for $(f_{5/2},g_{9/2})_{7^-}$, $(g_{9/2})^2_{8^+}$ and $(g_{9/2},d_{5/2})_{6^+}$ states in the fp shell and has been established at an earlier stage of the present experiment using a part of the data presented here.[49]

The WCM has been applied in the following way: The total energy of a nucleus A with p particles and h holes relative to a closed shell nucleus A_0 is given by

$$E(A)=E(A_0)+E(p)-E(h)+\langle ph|V_{ph}|ph\rangle\ . \tag{5}$$

$E(p)$ and $E(h)$ are the energies of p particles and h holes relative to $E(A_0)$. The values of $E(p)$ and $E(h)$ can be calculated from the experimental binding energies of the

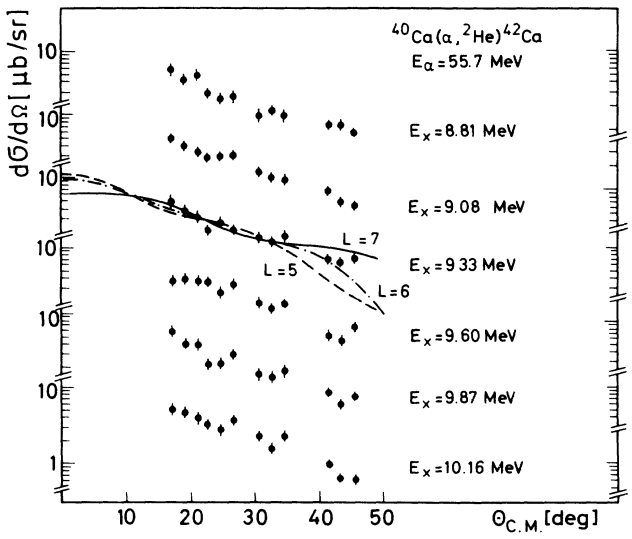

FIG. 39. Experimental angular distributions of transitions to states populated in the $^{40}\mathrm{Ca}(\alpha,{}^2\mathrm{He})^{42}\mathrm{Ca}$ reaction in the excitation energy region 8.8–10.2 MeV.

TABLE XXI. Experimentally assigned excitation energies of the 7^-, 8^+, and 6^+ *nn* high-spin states used for the shell-model calculations.

Nucleus	$(f_{5/2},g_{9/2})_{7^-}$ E_x (MeV)	$(g_{9/2})^2_{8^+}$ E_x (MeV)	$(g_{9/2},d_{5/2})_{6^+}$ E_x (MeV)
^{50}Ca	8.68[a]	10.33	9.80
^{52}Cr	7.75		
^{54}Cr	5.84	8.99	9.42
^{56}Cr	4.45	7.33	7.33
^{56}Fe	6.03	9.28	9.90
^{58}Fe	4.61	7.38	8.31
^{60}Fe	4.35	6.62	6.62
^{60}Ni	5.31	8.76	9.31
^{62}Ni	4.63	7.19	7.62
^{64}Ni	4.60	5.81	6.03
^{66}Ni	4.05	5.17	5.17
^{64}Zn[b]	4.64		
^{66}Zn	4.22	5.20	5.74
^{68}Zn	3.94	4.37	4.37
^{68}Ge[c]	4.05	4.84	
^{70}Ge[d]	3.96	4.21	
^{72}Ge	3.74	3.74	3.99

[a]Cross section weighted average of the 8.38 and 8.98 MeV states.
[b]Reference 36.
[c]Reference 35.
[d]Reference 34.

nuclei A_0, A_0+p, and A_0-h, if one assumes a weak coupling between the particles and the holes. Bansal and French give the following ansatz for the particle-hole interaction.[50]

$$\langle ph|V_{ph}|ph\rangle = -aph + b\mathbf{t}_p\mathbf{t}_h \ , \tag{6}$$

where a denotes the isoscalar two-body matrix element (TBME) $\langle j_p j_h^{-1}|V_{ph}|j_p j_h^{-1}\rangle$ averaged over all allowed values of J and T and b is the isovector strength describing the energy splitting for states with different isospin T.

After transformation to binding energies one obtains for a two-neutron state with spin J and $A = A_0+2-h$

$$B_{2n}(A_J,T) = B_{2n}((A_0+2)_J,T_0) - 2a(A_0+2-A)+b(T_A-1) \ . \tag{7}$$

A similar formula results for the corresponding one-neutron states

$$B_n(A_J,T) = B_n((A_0+1)_J,T_0) - a(A_0+1-A)-\frac{b}{2}(T_A-\tfrac{1}{2}) \ . \tag{8}$$

The parameters a and b are obtained for each configuration by a least-squares fit to the experimental data. In the calculations, the value $B((A_0+p)_J)$ is additionally treated as a free parameter, since the corresponding states $(A_0+p)_J$ are not known due to the lack of defined shell closure in the upper *fp*-shell mass region. However, with the large amount of data available this does not affect the accuracy of the values determined for a and b.

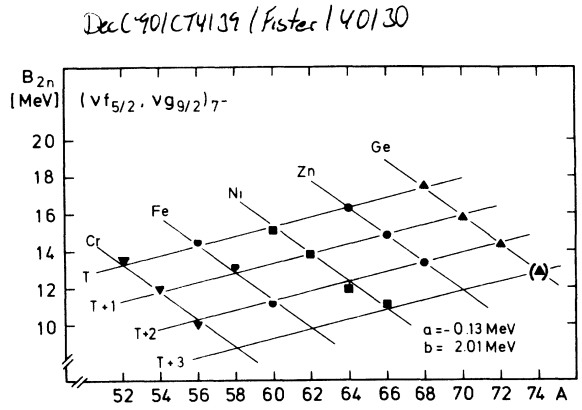

FIG. 40. Binding energies B_{2n} of the 7^- two-neutron states as a function of the mass number of the final nucleus A. The solid lines represent weak-coupling calculations explained in the text.

Figures 40–42 display the binding energies of the *nn* states versus the mass number of the final nucleus for the configurations $(f_{5/2},g_{9/2})_{7^-}$, $(g_{9/2})^2_{8^+}$ and $(g_{9/2},d_{5/2})_{6^+}$, respectively. The very systematic behavior is evident for all three configurations, and it is well reproduced by the WCM calculations. A similar quality of description is observed for the corresponding single-particle states shown in Fig. 43. The excitation energies are all known from studies of the (d,p) reaction (Ref. 23) and references therein).

The parameters a and b obtained for a *nn* configuration [e.g., $(f_{5/2},g_{9/2})_{7^-}$; $a=-0.13$ MeV, $b=2.01$ MeV] are (within a few percent) consistent with the average of the parameters describing the corresponding single-particle configurations $(f_{5/2},g_{9/2}$; $\bar{a}=-0.14$ MeV, $\bar{b}=1.87$ MeV). It is concluded that the linear A dependence of the *nn* binding energies is a consequence of the linear dependence of the corresponding single-particle binding energies. A similar agreement of the parameters a and b has been found for the binding energies of $(f_{7/2})^2_{6^+}$ and $f_{7/2}$ states in *sd* shell nuclei.[4]

The simple structure of the *n* and *nn* states is further

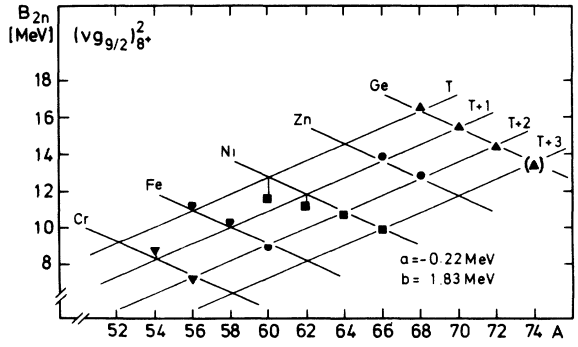

FIG. 41. Binding energies B_{2n} of the 8^+ two-neutron states as a function of the mass number of the final nucleus A. The solid lines represent weak-coupling calculations explained in the text.

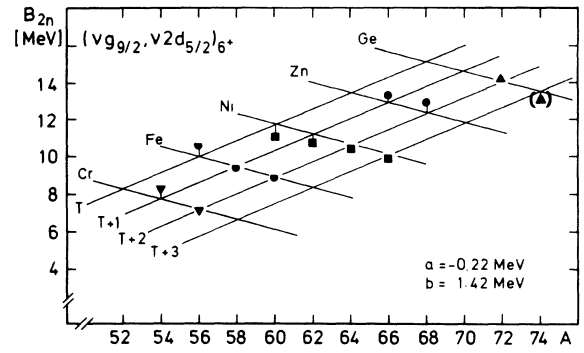

FIG. 42. Binding energies B_{2n} of the 6^+ two-neutron states as a function of the mass number of the final nucleus A. The solid lines represent weak-coupling calculations explained in the text.

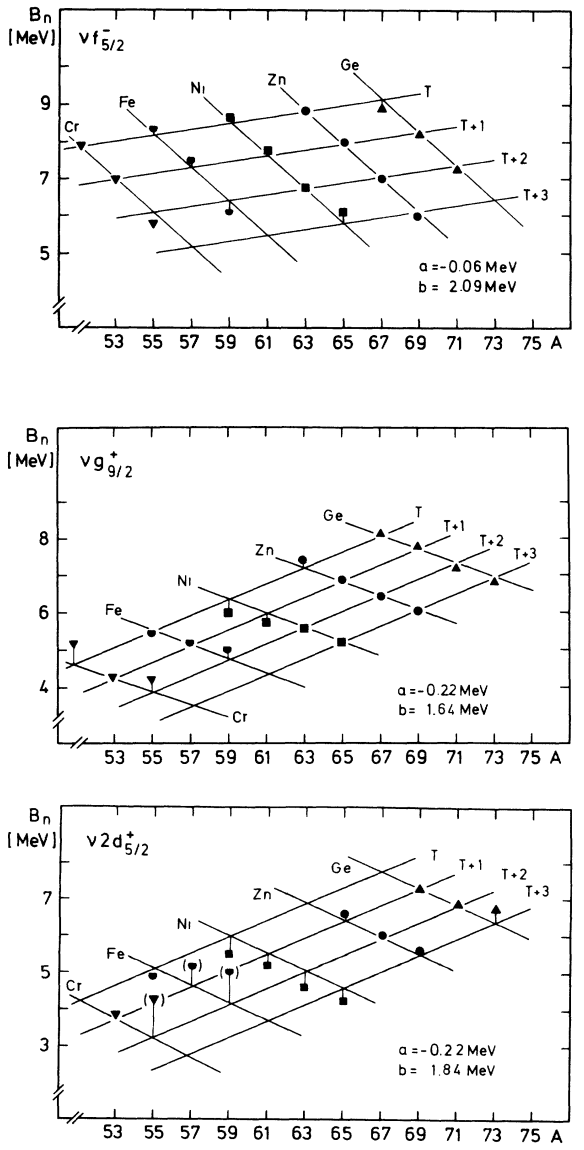

FIG. 43. Binding energies B_n of the $\frac{5}{2}^-$, $\frac{9}{2}^+$, and $\frac{5}{2}^+$ one-neutron states as a function of the mass number of the final nucleus A. The solid lines represent weak-coupling calculations explained in the text.

confirmed by the observed linear dependence on the isospin T. The WCM results exclude a significant isospin mixing, and T appears to be a good quantum number for these states. Due to the lack of definite isospin assignments in this mass region no absolute T values can be given for the states discussed in this study, but $T=T_Z$ is highly probable.

Since a definite assignment of T for one state would determine the absolute isospin values of all states shown in Figs. 40–43, results from the $(\alpha,{}^2\mathrm{He})$ reaction on the doubly magic nuclei ^{48}Ca with a well established g.s. isospin value are of special interest. A comparison of experimental and WCM values for the *nn* configurations and the corresponding single-particle transitions is given in Table XXII. The deviations for both *n* and *nn* states are significant, and it is evident that these states cannot be described by the WCM. The failure to reproduce the binding energies of the *nn* states is clearly correlated to the inability to describe the single-particle states; note that the differences observed for the corresponding *n* states roughly sum up to the differences resulting for the *nn* configurations. This might be understood from a consideration of the low-energy spectrum of ^{49}Ca which exhibits a different structure compared to other $N_n=29$ nuclei like ^{53}Cr and ^{55}Fe, in particular a large gap between the first- and second-excited state and almost equal excitation energies for the $f_{5/2}$ and the $g_{9/2}$ single-particle states.[52] While the other $N_n=29$ nuclei are described well by the WCM, this simple model, based on average interactions, is not valid to reproduce structure effects caused by the double shell closure in ^{48}Ca.

The good agreement with the experimental data makes the WCM model a powerful tool to predict presently unknown stretched *nn* configurations in fp-shell nuclei or to support tentative assignments. This is demonstrated for the nucleus ^{74}Ge where three dominant states were observed, but no clear distinction between the 6^+, 7^-, and 8^+ states could be given from the experimental results. The WCM clearly favors the speculative assignments indicated in Sec. IV A 11. The corresponding binding energies are shown in brackets in Figs. 40–42.

TABLE XXII. Comparison of the binding energies B of the experimentally assigned single-particle and stretched two-neutron configurations to predictions of the weak-coupling model described in the text.

Nucleus	Configuration	B_{expt} (MeV)	B_{calc} (MeV)
^{49}Ca[a]	$f_{5/2}$	1.22[b]	4.35
	$g_{9/2}$	1.11	1.74
	$d_{5/2}$	0.72	2.41
^{50}Ca	$(f_{5/2},g_{9/2})_{7^-}$	2.82[c]	6.71
	$(g_{9/2})^2_{8^+}$	1.17	2.65
	$(g_{9/2},d_{5/2})_{6^+}$	1.70	2.89

[a]Deduced from the excitation energies given in Ref. 52.
[b]Cross-section weighted-average binding energy of the states at 3.59 and 3.99 MeV excitation energy.
[c]Cross-section weighted-average binding energy of the states at 8.38 and 8.98 MeV excitation energy.

B. Crude shell model

The crude shell model (CSM), proposed by Chan *et al.*,[10] permits a very easy method to calculate the excitation energies of stretched two-nucleon states. It has been demonstrated that the CSM works well for the $(d_{3/2},f_{7/2})_{5^-}$ and $(f_{7/2})^2_{6^+}$ configurations selectively excited in the $(\alpha,^2\text{He})$ reaction on *sd*-shell nuclei.[10] For the data already presented in Ref. 49, Chan showed that the same applies for the *nn* configurations preferently populated by the $(\alpha,^2\text{He})$ reaction in the *fp*-shell mass region.[53]

The binding energy of a two-nucleon state $(j_1,j_2)_J$ in a final nucleus $A+2$ can be written as

$$B(A+2,(j_1,j_2)_J)=B(A+1,j_1)+B(A+1,j_2)+\langle j_1j_2|V_{\text{res}}|j_1j_2\rangle \ . \quad (9)$$

Here, $B(A+1,j_{1,2})$ denote the binding energies of the corresponding single-particle states and the two-body matrix element $\langle j_1j_2|V_{\text{res}}|j_1j_2\rangle$ takes into account the residual interaction of the two valence nucleons coupled to total spin J.

Converting binding energies to excitation energies one gets

$$E_x(A+2,(j_1j_2)_J)=E_x(A+1,j_1)+E_x(A+1,j_2)+\langle j_1j_2|V_{\text{res}}|j_1j_2\rangle+E_{\text{pair}} \ , \quad (10)$$

where E_{pair} stands for the pairing energy of the valence nucleons in the final $A+2$ nucleus and can be calculated from the g.s. binding energies of the nuclei A, $A+1$, and $A+2$. For the case of two neutrons E_{pair} is given by

$$E_{\text{pair}}(nn)=B(A,\text{g.s.})+B(A+2,\text{g.s.})-2B(A+1,\text{g.s.}) \ . \quad (11)$$

The residual interaction of aligned two-particle configurations is always small ($\ll 1$ MeV) for identical nucleons.[54] The CSM simply assumes

$$\langle j_1j_2|V_{\text{res}}|j_1j_2\rangle=0 \quad (12)$$

and Eq. (10) reduces to

$$E_x(A+2,(j_1j_2)_J)=E_x(A+1,j_1)+E_x(A+1,j_2)+E_{\text{pair}}(nn) \ . \quad (13)$$

The basic assumption of this approach is the excitation of pure configurations. This picture amounts to the supposition of a weak coupling between the particles and the holes in the WCM. Figures 44–46 depict a comparison of the experimentally observed excitation energies for the $(f_{5/2},g_{9/2})_{7^-}$, $(g_{9/2})^2_{8^+}$, and $(g_{9/2},d_{5/2})_{6^+}$ configurations to the results of Eq. (13). The diagonal lines correspond to the prediction of the CSM, and the deviation of data points from the lines is a direct measure of the effective residual interaction energy. With a few exceptions that will be discussed in more detail, the agreement between experimental and predicted values is good. Again, this finding underlines that rather pure *nn* configurations are preferentially excited in the $(\alpha,^2\text{He})$ reaction.

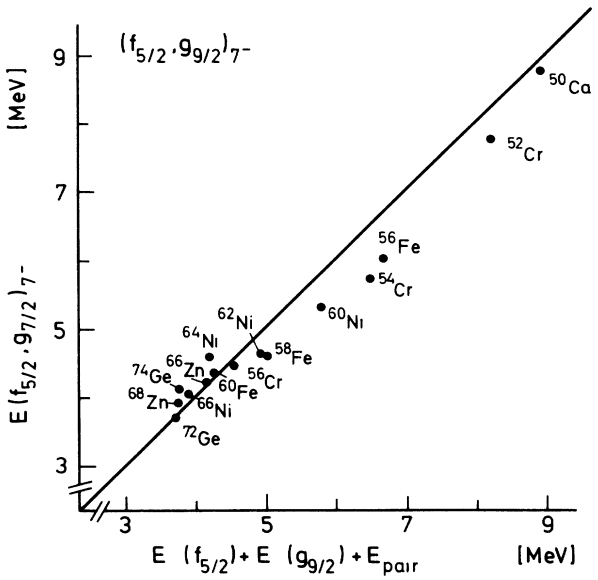

FIG. 44. Experimental excitation energies of the 7^- two-neutron states as a function of the calculated energies from the crude shell-model. See text.

As pointed out in Refs. 53 and 55, the link between WCM and CSM, which explains the mutual success of both models, is easily understood by inserting Eq. (8) in (9). With the neglection of the TBME, the CSM states that the WCM parameters for the two-particle configurations should be the average of the involved single-particle configurations. This coincides with the results obtained in the preceding section.

While the CSM accounts for most experimental results within ±0.5 MeV, marked deviations are observed for

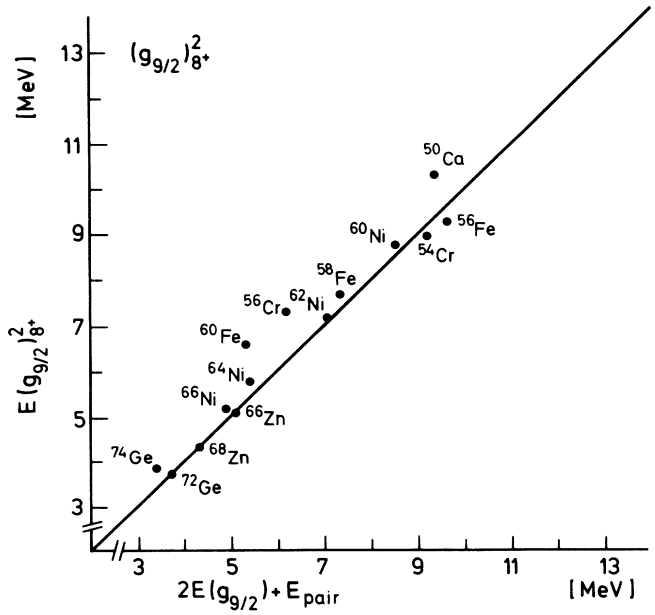

FIG. 45. Experimental excitation energies of the 8^+ two-neutron states as a function of the calculated energies from the crude shell-model. See text.

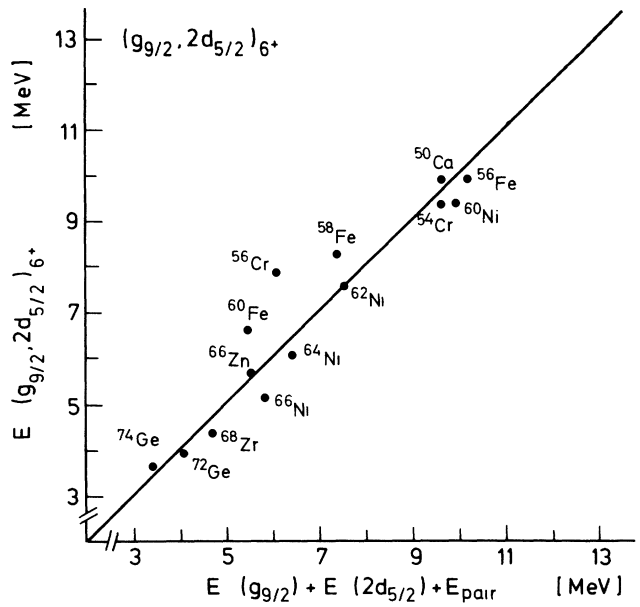

FIG. 46. Experimental excitation energies of the 6^+ two-neutron states as a function of the calculated energies from the crude shell-model. See text.

the $(g_{9/2})^2_{8^+}$ states in ^{50}Ca, ^{56}Cr, ^{60}Fe and the $(g_{9/2},d_{5/2})_{6^+}$ states in ^{56}Cr and ^{60}Fe. It should be noted that the lowest $g_{9/2}$ single-particle state in ^{49}Ca carries only a fraction of the spectroscopic strength ($S=0.30$) and little information exists about higher-lying states.[52] The excitation energies predicted by the CSM for the 8^+ and 6^+ states in ^{56}Cr and ^{60}Fe favor different assignments as obtained by the DWBA analysis. However, the good reproduction of these states by the WCM strongly supports the DWBA results. The deviations in the CSM might result from the coupling of the single-particle states to the core configurations which affects the excitation energies. On the other hand, the WCM description is independent of the target g.s. wave function.

Adapting the assumption of pure configurations, one can extract from Figs. 44–46 information about the experimental TBME of the 7^-, 8^+, and 6^+ states and compare these values to the information available[54,56] about residual interaction matrix elements. However, the reliability of this comparison is limited to cases where the single-particle states considered carry the main part of the strength and the configuration mixing is restricted to one major shell.[54] These conditions are best fulfilled for the $(g_{9/2})^2_{8^+}$ configuration in $^{60-66}$Ni and a resulting $T=1$ monopole interaction energy $E_J=(0.27\pm0.10)$ MeV is deduced, in agreement with the experimental value $E_J=0.23$ MeV evaluated from pickup experiments in the $A=90$ region[54] and the result $E_J=0.28$ MeV from an empirical effective interaction.[56] Taking into account all results of final nuclei above ^{56}Ni, a value $E_J=(0.13\pm0.15)$ MeV is obtained. This can be considered as a lower limit only, since the neglection of missing single-particle strength at higher excitation energy leads to a too attractive interaction energy.

Excluding all heavier final nuclei because of the filling of the $f_{5/2}$ shell, $E_J=(-0.36\pm0.28)$ MeV is deduced for the experimental results from ^{50}Ca to ^{62}Ni for the $(f_{5/2},g_{9/2})_{7^-}$ configuration. Restricting to strong single particle transitions, the result is $E_J=(-0.45\pm0.12)$ MeV for the final nuclei ^{56,58}Fe and ^{60,62}Ni. No results are given for the $(g_{9/2},d_{5/2})_{6^+}$ configuration, since the $d_{5/2}$ strength is considerably fragmented in all cases.

C. Shell-model calculations

The success of the simplified shell-model approaches discussed in the preceding sections indicates a very simple structure of the stretched nn states excited in the $(\alpha,^2He)$ reaction. The two-nucleon configurations seem to be rather pure, i.e., coupling to core excitations is negligible. This assumption will be tested more rigorously by comparing our data with large model space shell-model calculations which were performed not using our experimental results as input.

Due to the large configuration spaces involved, calculations in the fp shell are restricted to nuclei near closed shells or states whose wave functions can be approximated well by reduced shell-model spaces. Therefore, two different paths [called (a) nd (b) hereafter] were followed.

(a) Two selected regions ($^{57-66}$Ni and $^{52-56}$Cr+$^{54-58}$Fe) were studied in a configuration space, which should permit a satisfactory description of the properties of the g.s. and low-lying levels. Then the wave functions of the 7^- and 8^+ states should give detailed information on the degree of configuration mixing. Neutron shell-model orbits included were $(p_{3/2})^4$, $(p_{1/2})^2$, $(f_{5/2})^6$, and $(g_{9/2})^2$, where the upper index gives the maximum number of active nucleons in the respective orbit. The Cr and Fe isotopes were calculated relative to ^{48}Ca as inert core and the additional 4 (Cr) to 6 (Fe) protons were restricted to the $f_{7/2}$ orbit, while ^{56}Ni was assumed as inert core for the Ni isotopes. Despite the reduction of the $g_{9/2}$ occupation number and the neglection of higher-lying proton shells, calculations could not be performed completely for ^{56}Cr and ^{58}Fe, because the diagonalization matrices for several J^π values exceeded our computer capacities (the largest manageable matrices were $\approx 2500\times2500$).

(b) For a survey the calculations were performed for several groups of nuclei with respect to different inert cores (^{40}Ca for Ca isotopes, ^{48}Ca for Cr and Fe isotopes, ^{56}Ni for Ni and Zn isotopes). Above the assumed cores, *all* proton and neutron fp shell states plus the neutron $g_{9/2}$ state were included. The seniority of the resulting states was restricted to $S=2$ for even-even and $S=1$ for odd-even nuclei. Arguments that this rather severe truncation of the model space still allows information on the structure of the high-spin states will be given in the discussion.

For the determination of the TBME the schematic modified surface delta interaction (MSDI) was chosen which is given by[57]

$$V_{\mathrm{MSDI}}=-4\pi\delta(\mathbf{r}_i-\mathbf{r}_j)\delta(r_i-R_0)A_T+B(\tau_i\cdot\tau_j)\,. \qquad (14)$$

Here, $\mathbf{r}_i,\mathbf{r}_j$ and τ_i,τ_j denote the position vectors and the

isospins of the interacting particles i,j and R_0 stands for the radius of the nucleus. The interaction strength A depends on the relative spin coupling that is directly correlated to the isospin T of the two-nucleon system for a delta force. For a given T the values of different two-body matrix elements are completely fixed by the angular momentum algebra.[58] The empirical isospin term B acts on the diagonal matrix elements only; i.e., it leads to a shift of the binding energies.

The computer code RITSSCHIL[59] was used for the calculations, which were performed in a proton-neutron formalism. The MSDI parameters together with the single-particle energies were evaluated from fits to low-lying states of the considered nuclei. The inclusion of the corresponding odd-even nuclei was found to be important in order to reasonably establish the single-particle energies. Data from the experimentally observed high-spin states were *not* included in the fits. Tables XXIII and XXIV summarize the fit results for the model spaces (a) and (b), respectively.

For configuration space (a), complete spectra of the even-even nuclei up to $J=8$ and odd-even nuclei up to $J=\frac{9}{2}$ were calculated with the parameters listed in Table XXIII. The results for ^{56}Fe and ^{60}Ni are displayed in Figs. 47 and 48 as examples. All experimental and calculated levels are shown up to $E_x \approx 4$ MeV. At higher excitation energies, the level density is very large. So the results shown are restricted to a comparison of the experimentally deduced 7^- and 8^+ states to the lowest 7^- and 8^+ levels in the calculations. In addition, spectroscopic factors for one-neutron transfer to the odd-even nuclei were calculated in order to test the resulting wave functions. Finally, two-neutron transfer amplitudes were deduced for the transitions to the high-spin states.

TABLE XXIII. Single particle energies and MSDI parameter obtained for the fits for configuration space A.

Nuclei	$^{52-55}$Cr $^{54-58}$Fe	$^{57-66}$Ni
Inert core	^{48}Ca	^{56}Ni
fit levels	43	67
	Single-particle binding energies (MeV)	
$\nu g_{9/2}$	−0.80	−6.43
$\nu p_{1/2}$	−3.88	−9.20
$\nu f_{5/2}$	−3.52	−9.54
$\nu p_{3/2}$	−4.12	−10.20
$\pi f_{7/2}$	−16.98	
	MSDI parameter (MeV)	
A_1	0.60	0.54
A_0	0.18	
B	0.51	0.46
$Q_{\rm rms}$[a]	0.22	0.16

[a] $Q_{\rm rms}$ denotes the root mean square standard deviation.

The calculated spectra for $^{57-66}$Ni are very similar to the results of Koops and Glaudemans,[60] who performed a calculation of these nuclei using MSDI for the two-body interactions, but without the $g_{9/2}$ shell. The influence of the $g_{9/2}$ orbit on the low-energy regions seems to be small, and the differences probably mainly arise from the inclusion of a few additional states into the fit. The agreement of our calculations with experimental results is satisfying for all spectra and the spectroscopic factors of low-lying one-neutron transitions in the odd-even nu-

TABLE XXIV. Single-particle energies and MSDI parameter obtained from the fits for configuration space B.

Nuclei	$^{41-47}$Ca	$^{48-50}$Ca	$^{52-55}$Cr $^{54-60}$Fe	$^{57-66}$Ni	$^{63-69}$Zn[a]
Inert core	^{40}Ca	^{40}Ca	^{48}Ca	^{56}Ni	^{56}Ni
fit levels	20	6	36	48	23
			Single-particle binding energies (MeV)		
$\nu g_{9/2}$	−3.38	−3.63	−1.59	−6.76	−7.50
$\nu p_{1/2}$	−5.43	−6.50	−4.31	−9.24	−9.70
$\nu f_{5/2}$	−5.50	−4.94	−4.20	−9.53	−9.94
$\nu p_{3/2}$	−6.44	−8.44	−4.78	−10.35	−9.96
$\nu f_{7/2}$	−8.56	−10.18			
$\pi p_{1/2}$			−14.43		−9.70
$\pi f_{5/2}$			−15.41		−9.94
$\pi p_{3/2}$			−16.15		−9.96
$\pi f_{7/2}$			−16.79		
			MSDI parameter (MeV)		
A_1	0.39	0.32	0.35	0.40	0.41
A_0			0.18		0.27
B	0.12	0.48	0.49	0.41	0.52
$Q_{\rm rms}$[b]	0.19	0.09	0.28	0.25	0.30

[a] Neutron and proton single particle energies were kept equal in the Zn fit in order to reduce the number of free parameters.

[b] $Q_{\rm rms}$ denotes the root mean square standard deviation.

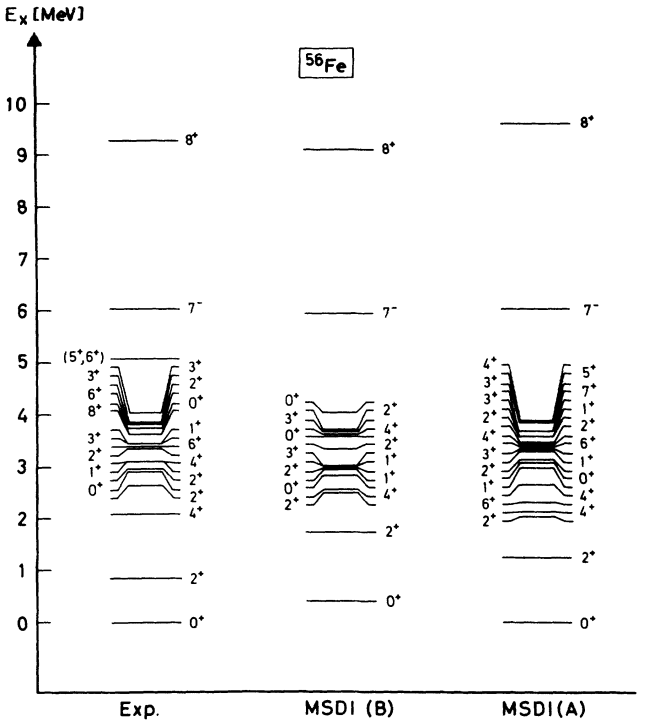

FIG. 47. Experimental level scheme of ^{56}Fe compared to results of shell-model calculations. The differences between model spaces A and B are explained in the text.

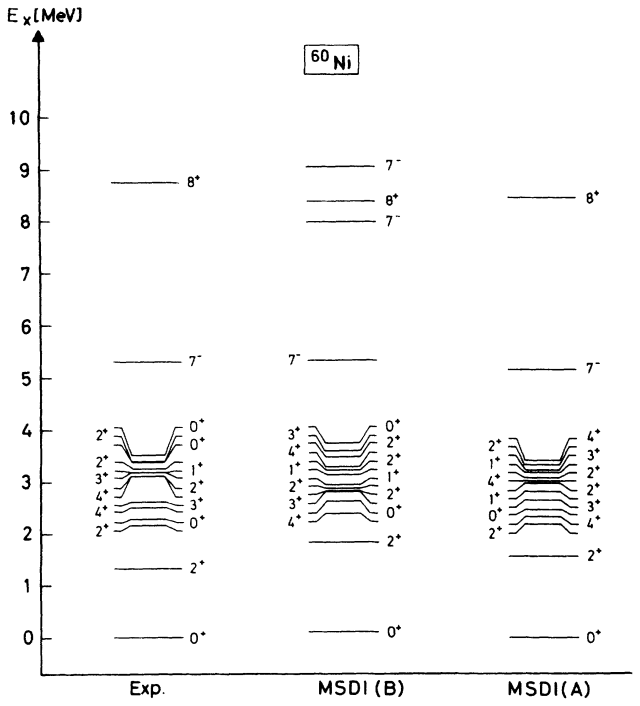

FIG. 48. Experimental level scheme of ^{60}Ni compared to results of shell-model calculations. The differences between model spaces A and B are explained in the text.

clei.[61] The spectra of $^{52-55}$Cr and $^{54-58}$Fe are reproduced somewhat poorer and one-neutron transfer spectroscopic factors tend to underestimate the degree of spreading, but basic features such as g.s. binding energies and spectroscopic factors of dominant single-particle states are described fairly well.[61] The deviations can be explained by the truncation induced by the selected model space and the limitations of the MSDI approach when the $f_{7/2}$ shell dominates the spectroscopic properties.[62,63]

Based on this check of the shell-model wave functions, spectroscopic factors for a transfer of $(f_{5/2},g_{9/2})_{7^-}$ and $(g_{9/2})^2_{8^+}$ nn configurations were calculated. These spectroscopic factors describe the overlap of the 7^- and the 8^+ states in the final nucleus $A+2$ with a $A_{\mathrm{g.s.}}\otimes(f_{5/2},g_{9/2})_{7^-}$ and $A_{\mathrm{g.s.}}\otimes(g_{9/2})^2_{8^+}$ coupling, respectively. Excitation energies and transfer strengths of the 7^- and 8^+ levels with the largest amplitudes are listed in Table XXV together with the summed transfer strengths

TABLE XXV. Excitation energies and spectroscopic factors S of 7^- and 8^+ states with dominant $(f_{5/2},g_{9/2})_{7^-}$ and $(g_{9/2})^2_{8^+}$ configurations calculated in model space A. ΣS gives the total $(f_{5/2},g_{9/2})_{7^-}$, respectively, $(g_{9/2})^2_{8^+}$ transfer strength of all calculated 7^- and 8^+ states.

		Expt.	MSDI		
Nucleus	J^π	E_x (MeV)	E_x (MeV)	S	ΣS
^{54}Cr	7^-	5.84	6.04	0.74	1.00
^{56}Fe		6.03	6.00	0.87	1.00
^{58}Fe		4.61	4.73	0.79	0.94
^{60}Ni		5.31	5.26	0.76	0.89
^{62}Ni		4.63	4.45	0.60	0.73
^{64}Ni		4.60	3.82	0.48	0.56
^{66}Ni		4.05	3.86	0.34	0.38
^{54}Cr	8^+	8.99	9.48	0.86	1.00
^{56}Fe		9.28	9.57	0.92	1.00
^{60}Ni		8.76	8.57	0.88	1.00
^{62}Ni		7.19	7.26	0.86	1.00
^{64}Ni		5.81	6.01	0.85	1.00
^{66}Ni		5.17	5.31	0.85	1.00

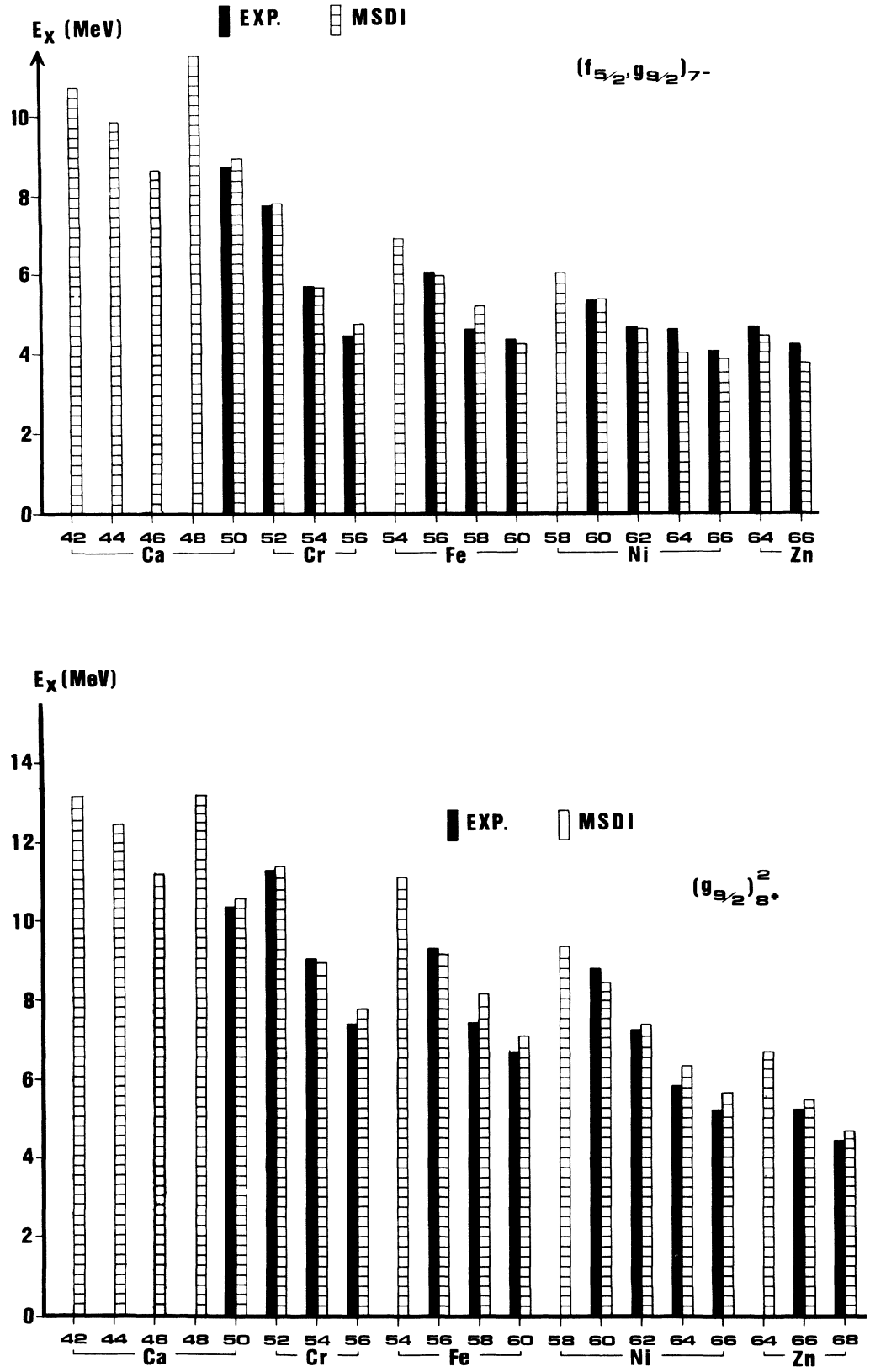

FIG. 49. Excitation energies of experimentally assigned $(f_{5/2},g_{9/2})_{7^-}$ and $(g_{9/2})^2_{8^+}$ states compared to shell-model results obtained for configuration space *B*.

of the $(f_{5/2},g_{9/2})_{7^-}$ and $(g_{9/2})^2_{8^+}$ configurations. No values could be extracted for the 8^+ states in ^{58}Fe, because the diagonalization of the 8^+ space exceeded our computer capacities. The excitation energies of the *nn* high-spin states are reproduced well with exception of the 7^- level in ^{64}Ni. Only a small configuration mixing is observed in all cases which supports the picture of rather pure *nn* configurations. The decrease of transfer strength for the 7^- levels in the heavier Ni isotopes is no contradiction to this statement, since the total $(f_{5/2},g_{9/2})_{7^-}$ strength decreases proportionally due to the filling of the $f_{5/2}$ shell with increasing neutron numbers.

The results for configuration space (b) are in reasonable agreement with the level schemes obtained with model space (a).[64] Typical examples of this comparison are displayed in Figs. 47 and 48. Although the restriction to seniority $S=2$ in model space (b) is certainly not appropriate for a detailed description of the low-lying part of the spectra, the energies of dominant single- and two-particle states should be reproduced fairly well. The determination of the single-particle energies and MSDI parameters of course depends on the low-lying states, but the inclusion of the odd-even nuclei and the large number of fit levels seem to average out the deviations and reasonable parameters compared to model space (a) are extracted.

The excitation energies of calculated 7^-, 8^+ levels with dominant $A_{\mathrm{g.s.}}\otimes(f_{5/2},g_{9/2})_{7^-}$, $A_{\mathrm{g.s.}}\otimes(g_{9/2})^2_{8^+}$ configurations are depicted in Fig. 49 together with the experimental results. All experimentally observed 7^- and 8^+ states are reproduced satisfactorily within ± 500 keV.

It is interesting to note that an almost constant MSDI isospin interaction strength $B\approx 0.5$ MeV results from the fits with both configuration spaces (excluding the lighter Ca isotopes). This value agrees well with the results from the weak coupling model $b[(f_{5/2},g_{9/2})_{7^-}]=2.01$ MeV and $b[(g_{9/2})^2_{8^+}]=1.83$ MeV taking into account the different definition of the isospin term for the MSDI $[B(\tau_1\cdot\tau_2)]$ and the WCM $[b(t_1\cdot t_2)]$.

VI. SUMMARY

The $(\alpha,{}^2\mathrm{He})$ reaction has been studied at about 56 MeV incident energy over a wide range of fp-shell nuclei. The use of large-area position-sensitive counters and a detector geometry that takes advantage of the *pp* final-state interaction enabled the measurement of angular distributions for the prominent transitions observed. The angular distributions were analyzed in the framework of zero-range DWBA using optical potentials extracted from the simultaneously recorded elastic α-scattering and an energy-, mass-, and charge-dependent parameter set for deuteron scattering.[22] In the outgoing channel, the depth of the real part was increased by 10 MeV to account for the double charge of the ^{2}He compared to a deuteron. The necessity of this correction stems from the nonlocality of the optical potential.

For target nuclei with a closed $f_{7/2}$ neutron shell, a pronounced selectivity of the $(\alpha,{}^2\mathrm{He})$ reaction to populate *nn* high-spin states with angular momentum $L\geq 5$ was observed. In particular, transitions with $(f_{5/2},g_{9/2})_{7^-}$, $(g_{9/2})^2_{8^+}$ and $(g_{9/2},d_{5/2})_{6^+}$ character could be identified in all cases from the shape and strength of the angular distributions and the ordering of the corresponding single particle levels. With the $f_{7/2}$ shell open, the increased number of final states and the fragmentation of the $f_{5/2}$, $g_{9/2}$, and $d_{5/2}$ single-particle states inhibited unambiguous J^π assignments for most levels. On the other hand, a selective excitation of the $(f_{7/2})^2_{6^+}$ configuration was seen for these nuclei.

The binding-energy systematics of the experimentally identified 7^-, 8^+, and 6^+ states were investigated. A linear dependence on the mass number A and the isospin T was observed for these states. This behavior is well described by the weak-coupling model.[49] Furthermore, the parameters a and b entering the calculations agree to within a few percent with the average values of the respective single-particle states, which show a similar systematic behavior. It is concluded that the linear A and T dependence of the binding energy of the *nn* states is a consequence of the linear behavior of the binding energy of the single-particle states.

In addition, the experimentally deduced excitation energies of the fully stretched *nn* configurations were compared with a crude shell model, which states that these energies can be described by the sum of the excitation energies of the corresponding single-particle states plus the pairing energy of the two neutrons.[53] Reasonably good agreement was observed for most states.

The success of both models indicates a very simple structure of the experimentally excited *nn* high-spin states, where the two transferred neutrons are coupled to maximum spin above an unperturbed core. The coupling to core excitations seems negligible.

Additional tests were done by large configuration-space shell-model calculations for Cr, Fe, and Ni isotopes. The two-body interaction was parametrized with the MSDI approach. Data from odd-even nuclei were included in the fits of the single-particle energies and MSDI strength parameters. The level schemes at low-excitation energies were reproduced satisfactorily, and the resulting wave functions permitted a calculation of spectroscopic factors, which were in reasonable agreement with data obtained from one-neutron transfer reactions.[61] Although not included in the fits, the excitation energies of experimentally observed 7^- and 8^+ states were described well and extracted spectroscopic amplitudes for two-neutron transfer into $(f_{5/2},g_{9/2})_{7^-}$ and $(g_{9/2})^2_{8^+}$ configurations corroborate the pure structure of these states. Based on this finding, calculations in a model space restricted to one- and two-particle configurations were performed for the major part of the experimentally covered mass region.[64] Again, the excitation energies of the lowest 7^- and 8^+ levels correspond well to the experimental results.

Empirical TBME were extracted for the $(f_{5/2},g_{9/2})_{7^-}$ and $(g_{9/2})^2_{8^+}$ configurations. The value obtained for

$(g_{9/2})^2_{8^+}$ agrees with results from pickup experiments[54] and systematics.[56]

In conclusion, the $(\alpha,{}^2\mathrm{He})$ reaction is a very powerful tool for the study of stretched two-neutron states. Due to their simple structure, an experimental knowledge of these states yields a sensitive test for nuclear structure studies. Experiments might be extended to even heavier target nuclei. A selectivity similar to that found in this study was reported for the $^{90}\mathrm{Zr}(\alpha,{}^2\mathrm{He})^{92}\mathrm{Zr}$ reaction[5] and recently for the $^{208}\mathrm{Pb}(\alpha,{}^2\mathrm{He})^{210}\mathrm{Pb}$ reaction.[65]

ACKNOWLEDGMENTS

We would like to thank the technical staff of the Bonn cyclotron for their support during the experiments and H. Hodde for preparing the targets. The help of J. Bisplinghoff in the early stages of the experiments is gratefully acknowledged. We are indebted to B. C. Metsch for his assistance in the shell-model calculations and valuable discussions. This work was supported by the Bundesministerium für Forschung und Technologie of the Federal Republic of Germany.

*Present address: Institut für Kernphysik, Technische Hochschule Darmstadt, D-6100 Darmstadt, Federal Republic of Germany.

†Present address: TRIUMF, Vancouver, British Columbia, Canada V6T 2A3.

[1]H. Langevin-Joliot, V. Datar, E. Gerlic, J. van der Wiele, F. Azaiez, S. Fortier, S. Gales, J. Guillot, J. M. Maison, C. P. Massolo, G. Duhanel, and G. Perrin, Phys. Rev. C **38**, 1168 (1988).

[2]R. Jahn, G. J. Wozniak, D. P. Stahel, and J. Cerny, Phys. Rev. Lett. **37**, 812 (1976).

[3]R. J. de Meijer, R. Kamermans, J. van Driel, and H. P. Morsch, Phys. Rev. C **16**, 2442 (1977).

[4]R. Jahn, D. P. Stahel, G. J. Wozniak, R. J. de Meijer, and J. Cerny, Phys. Rev. C **18**, 9 (1978).

[5]J. van Driel, R. Kamermans, and R. J. de Meijer, Nucl. Phys. **A350**, 109 (1980).

[6]N. Anyass-Weiss, J. Cornell, P. S. Fisher, P. N. Hudson, A. Menchaka-Rocha, D. J. Millener, A. D. Panagiotou, D. K. Scott, D. Strottman, D. M. Brink, B. Buck, and T. Engeland, Phys. Rep. **12C**, 201 (1974).

[7]M. Hamm and K. Nagatani, Phys. Rev. C **17**, 586 (1978).

[8]C. C. Lu, M. S. Zisman, and B. G. Harvey, Phys. Rev. **186**, 1086 (1969).

[9]U. Fister, R. Jahn, P. von Neumann-Cosel, P. Schenk, T. K. Trelle, D. Wenzel, and U. Wienands (submitted to Nucl. Phys. A).

[10]T. U. Chan, M. Agard, J. F. Bruandet, and C. Morand, Phys. Rev. C **19**, 244 (1979).

[11]B. J. Morton, E. E. Gross, E. V. Hungerford, J. J. Malafiny, and A. Zucker, Phys. Rev. **169**, 825 (1968).

[12]J. G. Rogers, M. Jain, and J. D. Bronson, Phys. Rev. C **8**, 961 (1973).

[13]K. M. Watson, Phys. Rev. **88**, 1163 (1952).

[14]A. B. Migdal, Zh. Eksp. Teor. Fiz. **28**, 3 (1955) [Sov. Phys. JETP **1**, 2 (1955)].

[15]E. Laesgaard, Nucl. Instrum. Methods **162**, 93 (1979).

[16]D. P. Stahel, R. Jahn, G. J. Wozniak, and J. Cerny, Phys. Rev. C **20**, 1680 (1979).

[17]H. Fuchs, Nucl. Instr. Meth. **200**, 361 (1982).

[18]P. D. Kunz, University of Colorado Reports COO-533-606 and COO-533-613 (1969).

[19]J. Raynal, program MAGALI (unpublished).

[20]D. G. Madland, P. Schwandt, W. T. Sloan, B. Shapiro and P. P. Singh, Phys. Rev. C **9**, 1002 (1974).

[21]G. Igo, Phys. Rev. Lett. **1**, 72 (1958).

[22]F. Hinterberger, G. Mairele, H. Schmidt-Rohr, G. J. Wagner, and P. Turek, Nucl. Phys. **A111**, 265 (1968).

[23]C. M. Lederer and V. S. Shirley, *Table of Isotopes,* 7th ed. (Wiley, New York, 1978).

[24]B. F. Bayman and A. Kallio, Phys. Rev. **156**, 1121 (1967).

[25]N. Bendjabellah, J. Delauny, T. Nomura, and H. J. Kim, Phys. Rev. Lett. **36**, 1536 (1976).

[26]B. L. Cohen, C. L. Fink, J. B. Moorhead, and R. A. Moyer, Phys. Rev. **157**, 1033 (1967).

[27]K. C. McLean, S. M. Dalgliesh, S. S. Ipson, and G. Brown, Nucl. Phys. **A191**, 417 (1977).

[28]T. U. Chan, C. Morand, M. Agard, J. F. Bruandet, B. Chambon, A. Dauchy, D. Drain, A. Giorni, and F. Glasser, Phys. Rev. C **29**, 441 (1984).

[29]G. F. Neal, Z. P. Sawa, F. P. Venezia, and P. R. Chagnon, Nucl. Phys. **A280**, 161 (1977).

[30]F. R. Hudson and R. N. Glover, Nucl. Phys. **A189**, 264 (1972).

[31]M. Dojo, Phys. Rev. C **31**, 1691 (1985).

[32]J. F. Bruandet, B. Berthet, C. Morand, A. Giorni, J. P. Longequeue, and T. U. Chan, Phys. Rev. C **14**, 103 (1976).

[33]C. Morand, J. F. Bruandet, B. Chambon, A. Dauchy, D. Drain, A. Giorni, and T. U. Chan, Nucl. Phys. **A313**, 45 (1979).

[34]C. Morand, M. Agard, J. F. Bruandet, A. Giorni, J. P. Longequeue, and T. U. Chan, Phys. Rev. C **13**, 2182 (1976).

[35]A. P. de Lima *et al.*, Phys. Rev. C **23**, 213 (1981).

[36]G. F. Neal, Z. P. Sawa, and R. P. Chagnon, Nucl. Phys. **A295**, 351 (1978).

[37]A. E. MacGregor and G. Brown, Nucl. Phys. **A190**, 548 (1972).

[38]M. Matoba, Nucl. Phys. **A118**, 207 (1968).

[39]R. A. Brown, D. B. Fossan, J. M. McDonald, and K. A. Snover, Phys. Rev. C **9**, 1033 (1974).

[40]J. H. Bjerregaard, O. Hansen, O. Nathan, R. Chapman, S. Hinds, and R. Middleton, Nucl. Phys. **A103**, 33 (1967).

[41]W. W. Daehnick, R. D. Rosa, M. J. Spisak, R. E. Brown, E. R. Flynn, R. A. Hardekopf, and J. C. Peng, Bull. Am. Phys. Soc. **28**, 651 (1983).

[42]D. E. Alburger, Nucl. Data Sheets **42**, 369 (1984).

[43]G. Brown, A. Denning, and J. G. B. Haigh, Nucl. Phys. **A225**, 267 (1974).

[44]G. M. Crawley, P. S. Miller, G. J. Igo, and J. Kulleck, Phys. Rev. C **8**, 574 (1973).

[45]J. H. Bjerregaard and O. Hansen, Phys. Rev. **155**, 1229 (1967).

[46]I. Kanestrøm and H. Koren, Nucl. Phys. **A130**, 527 (1969).

[47]F. J. Eckle, H. Lenske, G. Eckle, G. Graw, R. Hertenberger, H. Kader, F. Merz, H. Nann, P. Schiemenz, and H. H. Wolter, Phys. Rev. C **39**, 1662 (1989).

[48]D. C. Kocher and W. Haeberli, Nucl. Phys. **A196**, 225 (1972).

[49]R. Jahn, U. Wienands, D. Wenzel, and P. von Neumann-

Cosel, Phys. Lett. **150B**, 331 (1985).
[50]R. K. Bansal and J. B. French, Phys. Lett. **11**, 145 (1964).
[51]L. Zamick, Phys. Lett. **19**, 580 (1965).
[52]W. D. Metz, W. D. Callender, and C. K. Bockelman, Phys. Rev. C **12**, 827 (1975).
[53]T. U. Chan, Phys. Rev. C **36**, 838 (1987).
[54]W. W. Daehnick, Phys. Rep. **96**, 319 (1983).
[55]R. Jahn, Habilitation thesis, University of Bonn (1985).
[56]J. P. Schiffer and W. W. True, Rev. Mod. Phys. **48**, 191 (1976).
[57]P. W. M. Glaudemans, P. J. Brussard, and B. H. Wildenthal, Nucl. Phys. **A102**, 593 (1967).
[58]B. J. Brussard and P. W. M. Glaudemans, *Shell-Model Applications in Nuclear Spectroscopy* (North-Holland, Amsterdam, 1977).
[59]D. Zwaarts, Comput. Phys. Commun. **38**, 365 (1985).
[60]J. E. Koops and P. W. M. Glaudemans, Z. Phys. A **280**, 181 (1977).
[61]P. von Neumann-Cosel, Ph.D. thesis, University of Bonn (1986).
[62]R. B. M. Mooy, P. W. M. Glaudemans, and A. G. M. van Hees, Phys. Lett. **105B**, 251 (1981).
[63]R. B. M. Mooy and P. W. M. Glaudemans, Z. Phys. A **312**, 59 (1983).
[64]U. Fister, Ph.D. thesis, University of Bonn (1988).
[65]Institut für Strahlen und Kernphysik (ISKP) Bonn, Annual Report 1985–87, p. 19.